3 Results & Discussion

3.1 Introduction

No single experimental technique can yield a full understanding of the chemical nature of HEDP or its conformers and/or their interactions in solution or with hydroxyapatite. NMR spectroscopy was used to study the chemical change that occurs as a function of pH. Raman spectroscopy was extensively used to study both the solid state of HEDP and HEDP in solution as a function of pH. The solid-state structural aspects of HEDP and its anhydrous form were investigated by single crystal and powder XRD methods, respectively, and speciation in solution was done using chemometrical methods. All these results and findings are presented in this chapter.

3.2 NMR Spectroscopy

3.2.1 ^{1}H, ^{13}C and ^{31}P nuclei

The observed chemical shifts in the ^{1}H and ^{13}C NMR spectra of HEDP·H_2O are easily assignable as a maximum of only three and two differentiable signals respectively is expected. As two of the three proton signals are of an acidic nature (the PO**H** and CO**H** protons), it would be expected that only one of the three (the C$\mathbf{H_3}$ protons) would be observed when measuring in D_2O as solvent. This was indeed observed and is confirmed by a previous report in the literature showing only a single proton chemical shift [1]. Using D_2O as a solvent would not have allowed anhydrous HEDP to be compared with HEDP·H_2O. Therefore, to observe the acidic protons for both anhydrous and monohydrate HEDP, the solvent was changed to DMSO-d_6 and dryness was confirmed by doing a blank run. As expected, the ^{13}C data were two signals in all cases, irrespective of the

solvent. All the NMR chemical shifts were assigned and coupling constants calculated; these can be found in Table 3-1.

The most notable feature is the change in the chemical shifts associated with the PO**H** and CO**H** protons for HEDP·H_2O and HEDP from 7.9 and 2.1 ppm to 10.1 and 5.7 ppm respectively, as measured in DMSO-d_6. This is attributed to the absence of dissolved crystal water in the anhydrous case. The chemical shifts in the ^{13}C NMR spectra do not differ significantly between the anhydrous and monohydrate HEDP when measured in DMSO-d_6. However, when the ^{13}C chemical shifts for HEDP·H_2O when measured in DMSO-d_6 are compared with those measured in D_2O, there is a significant change. The two observed ^{13}C signals shift from 69.3 and 19.9 ppm when measured in DMSO-d_6 to 79.6 and 28.6 ppm respectively when measured in D_2O. This dramatic change is attributed to the fact that in D_2O other less protonated forms are observed rather than only the H_4L form of HEDP, which one would be more likely to observe in DMSO-d_6. Even though this is not ideal, direct comparison of published solid-state ^{13}C NMR chemical shift data on HEDP [2] with those obtained in DMSO-d_6 seems to support this hypothesis as the published solid-state values of 70.1 and 17.1 ppm for the **C**OH and **C**H_3 nuclei respectively compare well with the values of 69.3 and 19.9 ppm obtained in DMSO-d_6. The ^{31}P chemical shift seems to be solvent dependent only as one goes from DMSO-d_6 to D_2O for HEDP, but a discrepancy noted during the comparison of the experimental data with the data published in the literature [1, 3] indicated that other factors, such as pH and therefore H_4L concentration, might contribute significantly to the position of the ^{31}P chemical shift in D_2O; this will be discussed in Section 3.2.2.

Table 3-1. ^{1}H, ^{13}C, ^{31}P NMR chemical shift (δ) and coupling constant (J) data for HEDP·H_2O and HEDP measured in A. DMSO-d_6 and B. D_2O as solvent

A. *DMSO-d_6*	HEDP·H_2O δ (ppm)	HEDP·H_2O J (Hz)	HEDP δ (ppm)	HEDP J (Hz)
PO**H**	7.9 (b)	-	10.1 (b)	-
CO**H**	2.1 (s)	-	5.7 (s)	-
C**H$_3$**	1.4 (t)	$^{3}J_{H,P}$ = 15.8	1.4 (t)	$^{3}J_{H,P}$ = 15.9
O**H$_2$**	3.8 (s)	-	-	-
COH	69.3 (t)	$J_{C,P}$ = 150.8	69.4 (t)	$J_{C,P}$ = 151.7
CH$_3$	19.9 (s)	-	19.9 (s)	-
P	25.2 (t)	$J_{P,C}$ = 148.8	25.1 (t)	$J_{P,C}$ = 149.8
B. *D_2O*				
PO**H**	-	-		
CO**H**	-	-		
C**H$_3$**	1.4 (t)	$^{3}J_{H,P}$ = 15.8		
COH	79.6 (t)	$J_{C,P}$ = 148.1		
CH$_3$	28.6 (s)	-		
P	21.7 (t)	$J_{P,C}$ = 150.0		

Geunin *et al*. [1] report that there are two ^{31}P chemical shift values for HEDP·H_2O at 25.3 and 18.7 ppm due to the fact that the two phosphonic acid groups are crystallographically non-equivalent in the solid state; one group is strongly hydrogen-bonded to the single molecule of H_2O found in the molecular unit. Therefore, in solution, it could be expected that the non-hydrogen-bonded ^{31}P solid-state chemical shift should be comparable, as in the ^{13}C case, to that of the single ^{31}P chemical shift observed in DMSO-d_6 solution, where both phosphonic acid groups are equivalent on the NMR timescale. The solid-state chemical shift value of 25.3 ppm does indeed correlate well with the chemical shift measured in DMSO-d_6 of 25.2 ppm, and confirms the non-hydrogen-bonded nature of the phosphonic acid groups in DMSO-d_6.

Similarly, the nature of the calcium dihydrate salt of HEDP, $CaH_2L{\cdot}2H_2O$, was investigated in both DMSO-d_6 and D_2O. $CaH_2L{\cdot}2H_2O$ is only sparingly soluble in both solvents, and therefore it was not possible to obtain ^{13}C NMR data. The NMR data that were obtained, as well as the coupling constants, can be found in Table 3-2. In this case the PO**H** and CO**H** protons were observed in D_2O for the

complex, indicating that their rate of proton exchange relative to the free-acid form of HEDP has changed sufficiently to be observed; this shows that this complex can be observed in the aqueous solution by means of solution NMR. Low solubility could account for the fact the PO**H** signals were not observed in DMSO-d_6. One would have hoped also to see a Ca-O**H$_2$** signal, but rapid D_2O exchange is probably the cause for it not having been observed. A similar change in the position of the ^{31}P chemical shift occurs for the $CaH_2L{\cdot}2H_2O$ complex as occurred with HEDP when moving from DMSO-d_6 to D_2O as solvent.

Table 3-2. ^{1}H, ^{13}C, ^{31}P NMR shift (δ) and coupling constant (J) data for $CaH_2L{\cdot}2H_2O$ measured in DMSO-d_6 and D_2O as solvent

$CaH_2L{\cdot}2H_2O$	DMSO-d_6		D_2O	
	δ (ppm)	J (Hz)	δ (ppm)	J (Hz)
PO**H**	-	-	8.4 (b)	-
CO**H**	1.2 (s)	-	2.0 (s)	-
C**H$_3$**	1.4 (t)	$^{3}J_{H,P}$ = 15.8	1.5 (t)	$^{3}J_{H,P}$ = 15.2
O**H$_2$**	3.7 (b)	-	-	-
P	25.2 (t)	-	21.7 (t)	-

3.2.2 pH-dependent ^{31}P and ^{23}Na NMR spectroscopy

The ^{31}P NMR data were collected for the solution series, prepared as described in Section 2.2, and the interaction of the Na^+(aq) ion was monitored by means of ^{23}Na NMR spectroscopy. The ^{23}Na chemical shift changed by only 0.9 ppm over the whole pH range. This shift is attributed to the increase in the solution's ionic strength as pH increases (due to the formation of highly charged species) rather than to the formation of hydroxo complexes, which form only above a pH value of 13.00 [4], or as a result of an interaction with HEDP.

Figure 3-1 shows the trend observed for the ^{31}P shift over the pH range. Obtaining the second derivative of this curve gives approximate values of the dissociation constants, pK_a, of the various protonated forms of HEDP, except for the H_4L/H_3L^- and H_3L^-/H_2L^{2-} which cannot be resolved by the NMR data. However, an average value was determined for the $H_4L \leftrightarrows H_3L^- \leftrightarrows H_2L^{2-}$ equilibrium. The second derivative-determined values compared with those from

Table 1-1 can be found in Table 3-3, and from this table it can be seen that they are in good agreement. The first POH deprotonation of each phosphonate group seems to have a shielding on the phosphorus nucleus. The second POH deprotonation still shows a shielding effect relative to the fully protonated H_4L, but not as efficient as mono-deprotonation, as the ^{31}P signal shifts downfield again with an increase in pH.

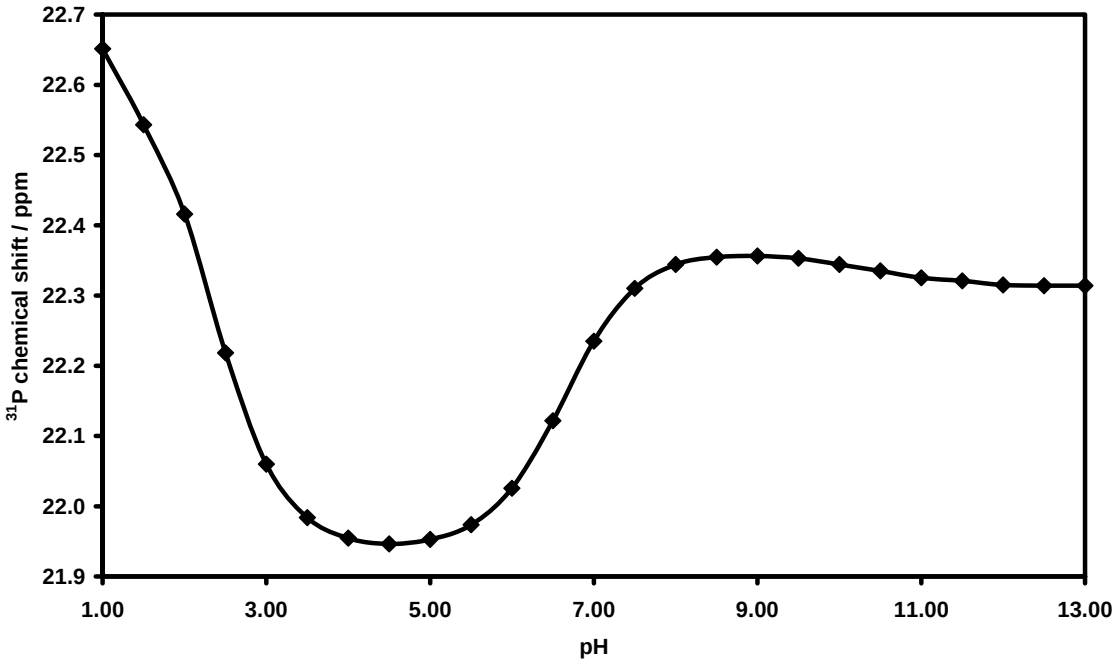

Figure 3-1. Variation in the ^{31}P chemical shift as a function of pH

Table 3-3. Comparison of reported pK_a values with pK_a values determined using the second derivative of the curve defined by the ^{31}P chemical shift as a function of pH for HEDP(aq)

Equilibrium reaction	pK_a †	pK_a ‡
$H_4L \leftrightarrows H_3L^- + H^+$	2.43	2.49
$H_3L^- \leftrightarrows H_2L^{2-} + H^+$	2.97	
$H_2L^{2-} \leftrightarrows HL^{3-} + H^+$	6.81	6.95
$HL^{3-} \leftrightarrows L^{4-} + H^+$	10.11	10.92

† From ref. [5]
‡ Determined from $f''(pH)$

3.3. Thermal gravimetric analysis

Figure 3-2 shows the first derivative curve of the weight percentage loss as a function of temperature, indicating that five major thermal events occur for HEDP upon heating.

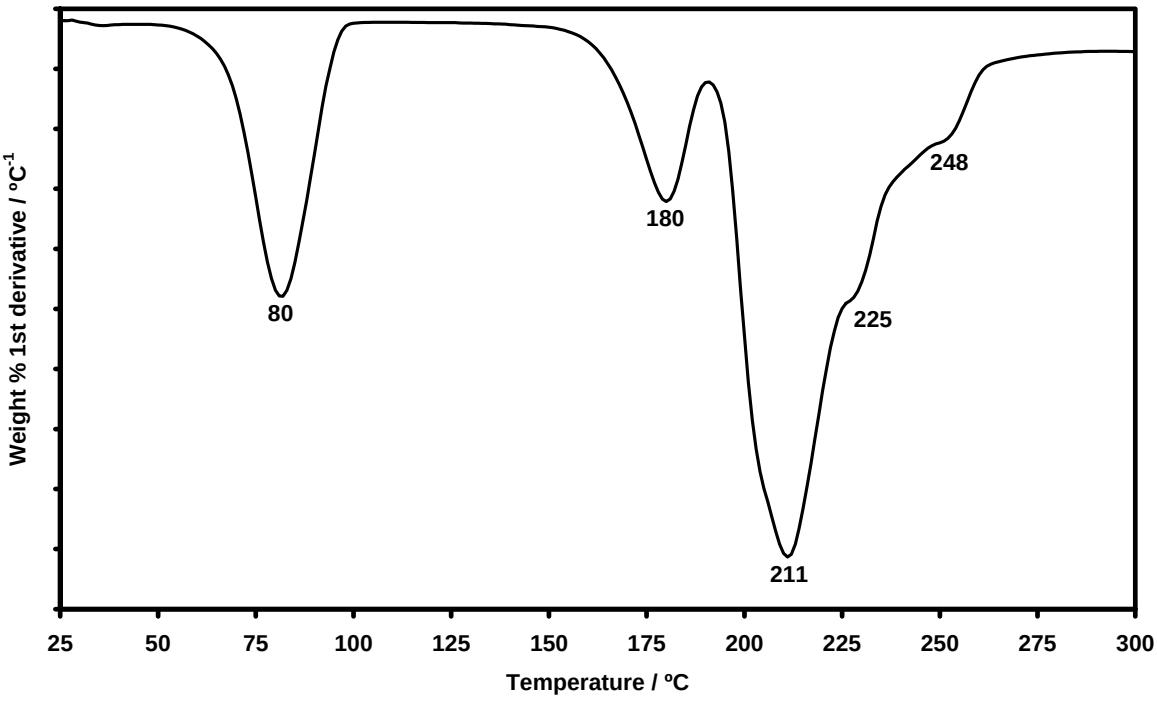

Figure 3-2. The first derivative curve of HEDP·H_2O for the temperature range 25 – 300 °C

The first event at 80 °C is the loss of the crystal water of hydration [6,7] and the second at 180 °C is the intermolecular loss of water to form a six-membered heterocyclic compound of which the derivative was isolated and a single crystal obtained [7]. The large bands at 211 °C and higher are reported to be phosphate and phosphate degradation products as a result of the breaking of the C-P bonds [6]. From this thermal gravimetric analysis the working temperature of 120 °C was chosen for anhydrous HEDP as this is above the dehydration temperature and would ensure that no surface-adsorbed water would be present as well.

3.4 X-ray diffraction methods

3.4.1 HEDP·H_2O

Uchtman and Gloss [8] were the first to report the single-crystal X-ray structure of HEDP in 1972, having an *R* value of 5.1%, but they were unable to determine accurately the hydrogen positions during this study. This is not unusual for bisphosphonate crystal structures [9]. Silvestre *et al*. [10] subsequently determined an accurate structure for HEDP·H_2O using neutron diffraction and reported this structure, as well as the hydrogen positions which they obtained by X-ray diffraction methods. Table 3-4 contains a summary of the crystallographic data as determined for the crystal structure. All other relevant data, bond lengths, bond angles and dihedral angles can be found in Table A-1 in the Appendix.

As a single molecular unit, HEDP (as H_4L) can have at most C_s as its highest point group symmetry. In the solid state, it adopts a C_1 conformation due to the very strong hydrogen bonding that occurs in the crystal structure [10]. This occurs in all other published structures containing any of the H_3L^-, H_2L^{2-}, HL^{3-} or L^{4-} forms of HEDP [9]. The molecular unit can be seen in Figure 3-3. Hydrogen bonding dominates the crystal lattice of HEDP·H_2O. The H_4L units generate a hydrogen-bonded network of two stacked two-dimensional staggered layers parallel to the *ac*-plane in the direction of the *b*-axis. These staggered H_4L layers are held together by a hydrogen-bonded layer of water molecules also parallel to the *ac*-face to complete the structure, as can be seen in Figure 3-4.

Table 3-4. Selected X-ray crystallographic data obtained for HEDP·H_2O

Empirical formula	$C_2 H_{10} O_8 P_2$	
Formula weight	224.04	
Crystal system	Monoclinic	
Space group	$P2_1/c$	
Unit cell dimensions	a = 6.9878(7) Å	α = 90º
	b = 17.5810(18) Å	β = 108.451(2)º
	c = 7.1140(8) Å	γ = 90º
Volume	829.05(15) Å^3	
Z	4	
Density (calculated)	1.795 g.cm^{-3}	
Final R indices ($I > 2\sigma(I)$)	R_1 = 0.0317, R_{w2} = 0.0844	
R indices (all data)	R_1 = 0.0319, R_{w2} = 0.0846	

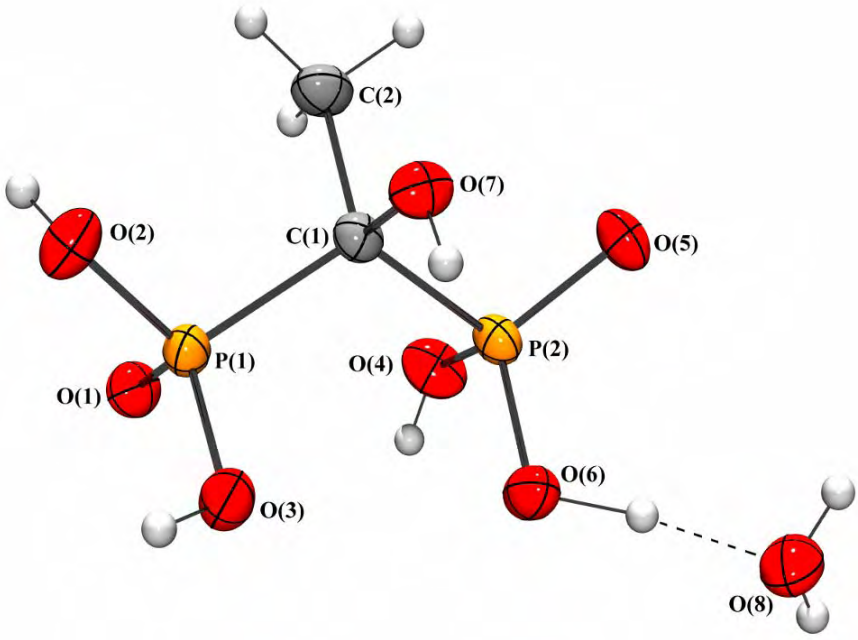

Figure 3-3. An Ortep/POV-ray drawing of the asymmetrical and molecular units of HEDP·H_2O. Ellipsoids are shown at the 50% probability level

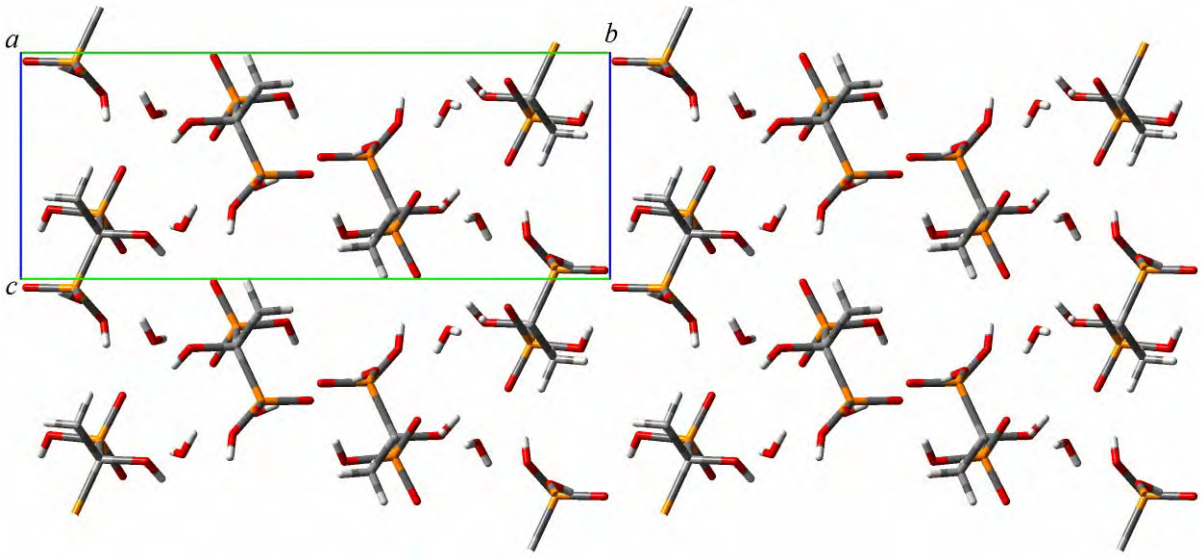

Figure 3-4. Expanded crystal lattice of HEDP·H_2O viewed along the *a*-axis

Table 3-5 lists notable hydrogen bond distances for HEDP as determined by X-ray diffraction in comparison with those determined by neutron diffraction methods [10]. Standard deviations are not included for ease of comparison, but can be found in Table A-1 in the Appendix. All standard deviations for values given in Table 3-5 range from 0.002 – 0.004 Å. The superiority of neutron over X-ray diffraction where hydrogen atoms are involved can be seen in the differences between the two sets of data, such as $d_{D–H}$, $d_{H\cdots A}$ and D$\hat{H}$A, but the accuracy of the X-ray data is obvious from the good agreement that exists for the two sets of data for the non-hydrogen atoms, such as $d_{D\cdots A}$ in Table 3-5 and the unit cell dimensions compared in Table 3-6.

The most notable hydrogen bond is the one that exists between H_2O and HEDP at P2-O6-H6···O8 where $d_{H6\cdots O8}$ = 1.40(4) Å (bold row in Table 3-5), making 06-H6 the longest PO-H bond in the HEDP molecule with $d_{O6\cdots H6}$ = 1.04(4) Å, compared with an average of 0.76 Å for the other PO-H bonds. In later sections it will be seen that the removal of crystal water is of significance in both the structural and spectral aspects of HEDP. The $d_{D–H}$ values differ the most between the X-ray and neutron data. This is due to the inherent difficulty of determining hydrogen bond distances accurately and is also reflected in the larger e.s.d values as seen in Table A-1.3 of the Appendix.

Table 3-5. Hydrogen bond data for HEDP·H_2O: X-ray (X) vs. neutron (N) data [10]

D-H…A	$d_{D–H}$ (Å)		$d_{H\cdots A}$ (Å)		$d_{D\cdots A}$ (Å)		DĤA (º)	
	X	N	X	N	X	N	X	N
O2-H2···O1*	0.77	1.003	1.84	1.604	2.615	2.604	177	176.4
O3-H3···O5**	0.77	1.046	1.72	1.437	2.483	2.476	169	172.7
O4-H4···O1***	0.73	0.999	1.90	1.622	2.623	2.617	170	174.0
O6-H6···O8	**1.04**	**1.121**	**1.40**	**1.317**	**2.435**	**2.437**	**173**	**175.8**
O7-H7···O5#	0.79	0.974	1.94	1.771	2.699	2.687	162	154.8
$O8\text{-}H8_A\cdots O7^{\#\#}$	0.76	0.984	1.95	1.737	2.696	2.697	166	164.5
$O8\text{-}H8_B\cdots O6^{\#\#\#}$	0.73	0.955	2.20	1.974	2.899	2.888	160	159.5

Symmetry transformations used to generate equivalent positions:
*: $-x, -y + 1, -z + 1$ **: $x, y, z + 1$ ***: $-x + 1, -y + 1, -z + 1$
#: $x, -y + 1.5, z + 0.5$ ##: $x + 1, y, z$ ###: $x, -y + 0.5, z - 0.5$

Table 3-6. HEDP·H_2O $P2_1/c$ unit cell comparison: X-ray vs. neutron data [10]

	X-ray	Neutron		X-ray	Neutron
a	6.9878(7) Å	6.983(9) Å	β	108.451(2)º	108.5(1)º
b	17.5810(18) Å	17.556(3) Å	V	829.05(15) $Å^3$	826.4 $Å^3$
c	7.1140(8) Å	7.109(9) Å	ρ	1.795 $g.cm^{-3}$	1.80 $g.cm^{-3}$

The O1=P1···P2=O5 dihedral is measured as 127.62º. As previously reported [10], when the C2-C1-P2-O5 dihedral is turned by ~120º such that the O1=P1···P2=O5 dihedral approximates 0º, one obtains a conformation (ignoring minor differences in the OH orientations) having C_s point group symmetry (Figure 3-5). It is also interesting to note that even though intermolecular hydrogen bonding dominates the structure, there is no hydrogen bonding between two water molecules or any significant intramolecular hydrogen bonding in HEDP.

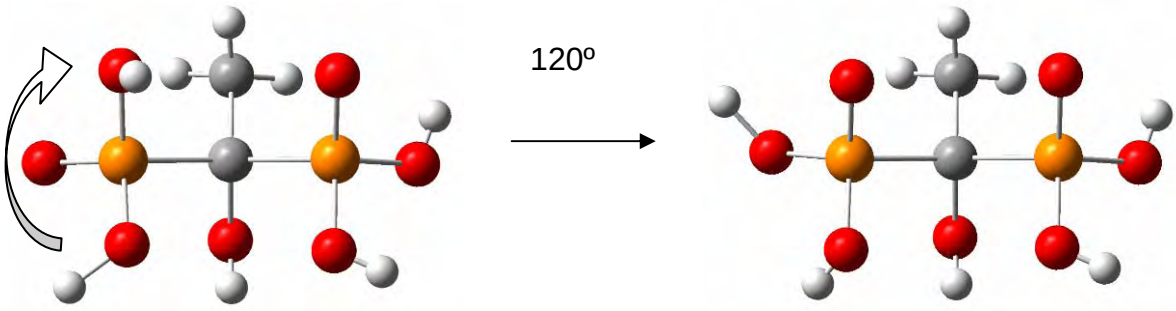

Figure 3-5. The HEDP can obtain pseudo C_s symmetry by rotation of one of the PO_3H_2 groups by ~120º

3.4.2 HEDP

Extensive attempts were made to obtain a single crystal of the anhydrous form of HEDP, but these were unsuccessful. Thus powder X-ray diffraction methods in conjunction with Rietveld analysis were employed to solve the structure. This has very successfully been done for organic molecular crystals having different phase transformations [11], including another bisphosphonate of importance to the pharmaceutical industry, namely risedronic acid (Figure 1-1E), that can have more than one hydrated state [12]. Figure 3-6 shows the powder X-ray diffraction patterns of HEDP·H_2O in comparison with the anhydrous HEDP to illustrate the definite structural rearrangement that occurs as one goes from the monohydrate to the anhydrous HEDP form.

TOPAS Academic [13] was used to index the unknown anhydrous HEDP powder pattern but, prior to this, two indexing sets with different cut-off criteria regarding reflection intensity (after normalisation) were performed on the known structure of HEDP·H_2O to validate the results and determine that the indexing could be accepted with confidence for the anhydrous HEDP. The two sets were: all reflections with an intensity above 10% (24 reflections) and all reflections above 15% (13 reflections) for the 2θ range 5 – 60º. Each indexing gave a ranked list of possible unit cell solutions, of which the top ten for both HEDP·H_2O (compared with its known structure) and HEDP can be found in Table 3-7 and Table 3-8 respectively. Indexing done using the 24-reflection set gave the most acceptable

results when compared with the experimental data for HEDP·H_2O. It is important to note that even though the correct space group for HEDP·H_2O is listed only as the third solution in Table 3-7, eight of the ten possible solutions' cell parameters correlate extremely well with the experimentally determined cell parameters of HEDP·H_2O.

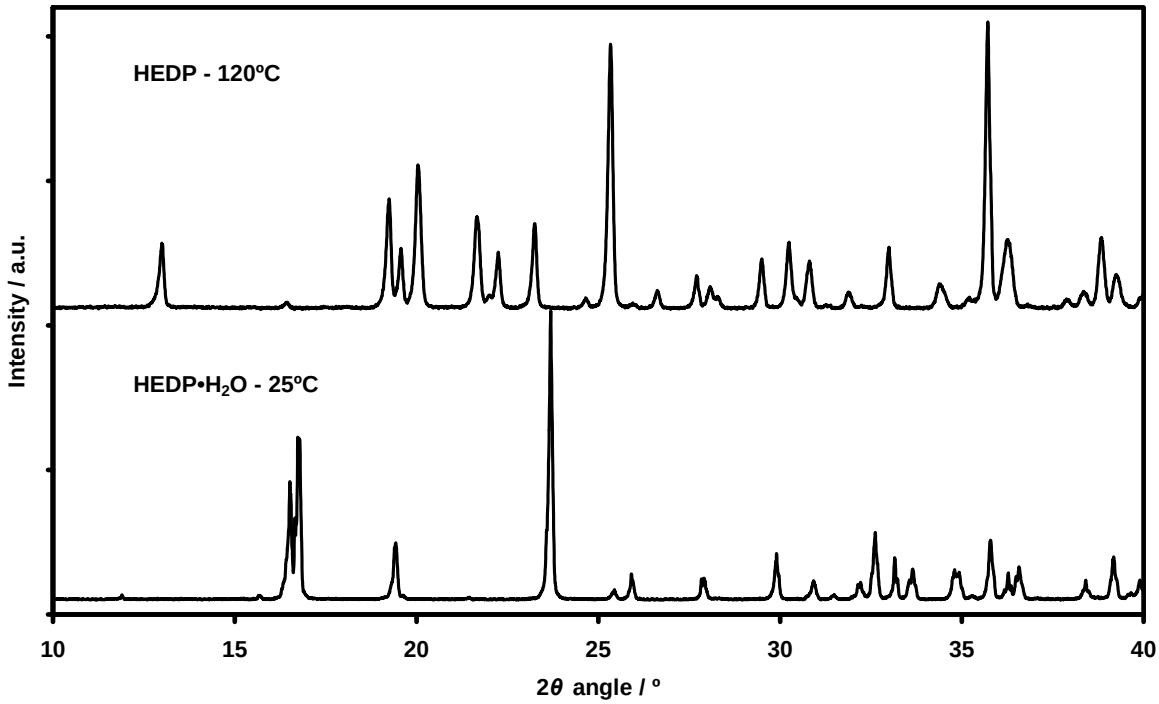

Figure 3-6. Powder XRD patterns of HEDP·H_2O and anhydrous HEDP showing that there is a structural difference between the two crystalline compounds

Table 3-7. The ten most probable index solutions (in Å and º) found for HEDP·H_2O compared with the experimental data displayed in bold at the top

Space Group HEDP·H_2O	Cell Volume	a	b	c	α	β	γ
$P2_1/c$	***829.05***	***6.9878***	***17.5810***	***7.1140***	***90***	***108.451***	***90***
$P2_1$	831.485	6.9987	17.5823	7.1238	90	108.462	90
$P2_1$	831.853	6.9988	17.5873	7.1246	90	108.458	90
$P2_1/c$	831.853	6.9988	17.5873	7.1246	90	108.458	90
$P2_1/c$	831.485	6.9987	17.5823	7.1238	90	108.462	90
$P2$	831.485	6.9987	17.5823	7.1238	90	108.462	90
$P2$	831.853	6.9988	17.5873	7.1246	90	108.458	90
~~$P2_1$~~	~~832.338~~	~~7.0000~~	~~17.5896~~	~~8.2586~~	~~90~~	~~125.061~~	~~90~~
Pc	831.853	6.9988	17.5873	7.1246	90	108.458	90
~~$P2_1/e$~~	~~832.338~~	~~7.0000~~	~~17.5896~~	~~8.2586~~	~~90~~	~~125.061~~	~~90~~
Pc	831.485	6.9987	17.5823	7.1238	90	108.462	90

Table 3-8. The ten most probable index solutions (in Å and º) found for HEDP

Space Group HEDP	Cell Volume	a	b	c	α	β	γ
$P2_1$	710.127	5.3981	10.3817	13.0550	90	103.925	90
$P2_1$	710.068	5.3980	10.3817	13.0542	90	103.923	90
$P2$	710.127	5.3981	10.3817	13.0550	90	103.925	90
$P2_1$	710.396	5.3992	10.3824	12.8720	90	100.089	90
~~$P2_1$~~	~~710.124~~	~~5.3981~~	~~10.3817~~	~~15.2804~~	~~90~~	~~123.978~~	~~90~~
$P2_1$	710.054	5.3979	10.3816	12.8701	90	100.100	90
$P2$	710.068	5.3980	10.3817	13.0542	90	103.923	90
$P2$	710.396	5.3992	10.3824	12.8720	90	100.089	90
~~$P2$~~	~~710.124~~	~~5.3981~~	~~10.3817~~	~~15.2804~~	~~90~~	~~123.978~~	~~90~~
$P2$	710.054	5.3979	10.3816	12.8701	90	100.100	90

The results for HEDP give four possible solutions based on the cell parameters. All solutions have the initial cell parameters: a = 5.398 Å, b = 10.382 Å, c = 12.962 Å combined with β = 100.10º or 103.92º in space group $P2_1$ or $P2$.

The two possibilities struck through in Table 3-8 were heuristically deemed to be less possible when compared with the other solutions.

A single water molecule has a calculated van der Waals' volume of ~17.5 Å^3 [14], resulting in the four water molecules in the HEDP·H_2O unit cell having a combined volume of 70 Å^3. Subtracting this from the experimentally determined cell volume of 829.05 Å^3 of HEDP·H_2O gives the volume of all H_4L units as 759.05 Å^3. Comparison of this value with that obtained for anhydrous HEDP of ~710 Å^3 from the indexing procedure shows that it would be valid to assume that four HEDP units are present within the unit cell of anhydrous HEDP. This implies that the asymmetrical unit should consist of two non-equivalent HEDP molecules as both $P2_1$ and $P2$ have Z = 2. The difference between the two calculated cell volumes containing only H_4L can be rationalised as resulting from the different packing geometry existing in the different cell structures in the anhydrous and monohydrate forms of HEDP and even as an 'interaction volume' between the water and H_4L molecules in the monohydrate case, which is not quantified here.

Both the Pawley and Le Bail powder XRD curve-fitting algorithms gave refinements, with an R_{wp} (mathematically defined in Eq. 1.22) between 6.44 and 7.44% for all space group and cell parameter combinations as stipulated earlier. It was therefore decided to continue with all four for the indicated structure determination as it was difficult to decide with confidence at this stage which unit cell parameter combination was the most likely.

A pseudo-Voigt function was selected to model the peak and background profiles of the experimental powder pattern as it approximates the Voigt function, which is a weighted summation of Gaussian and Lorentzian functions, adequately enough [15]. In the pseudo-Voigt case the width at half-maximum (FWHM) values for the Gaussian and Lorentzian functions are kept the same. All pseudo-Voigt variables and lattice parameters were further refined during the Pawley and Le Bail fittings and used as such to determine the rigid body structure.

The rigid body used in the structure refinement was generated from the single-crystal structure of HEDP·H_2O. Figure 3-7 shows the calculated,

experimental and difference XRD patterns for the four combinations of the cell parameters as obtained using the rigid body. Comparison of the indices of agreement R_{wp}, R_B and goodness of fit (GOF) in Table 3-9 for the $P2$ and $P2_1$ space groups shows that $P2_1$ is clearly the more plausible choice for the space group as the difference between the two sets is ~10% and the two most intense reflections experimentally obtained could not be adequately modelled in space group $P2$ (Figure 3-7). Unfortunately, no decision could yet be made on the β-angle value as the indices of agreement differ by less than 1% within the same space group. One reason could be that the low d-spacing values used during the initial indexing process could have introduced an error due to them being less accurate. Re-indexing was therefore attempted for d-spacing values greater than 2.5 Å, assuming that all lattice parameters are at least greater than 3 Å [16]. This resulted in a lowering of the space group symmetry, giving the cell as triclinic $P\bar{1}$ with a = 5.399 Å, b = 10.385 Å, c = 12.876 Å, α = 89.96º, β = 100.12º and γ = 90.02º. This correlates extremely well with the previously determined systems, and hinted at the β-angle being ~100.1º with $\alpha = \gamma$ = 90º. With $\alpha = \gamma$ = 90º, the $P\bar{1}$ space group transforms to $P2_1$.

An iterative refinement process was now followed using the rigid body for this unit cell, in which the cell parameters and rigid body positioning were alternately refined with each cycle until no further improvement in the indices of agreement was obtained. Figure 3-8 shows a perspective drawing of one filled unit cell obtained in this manner.

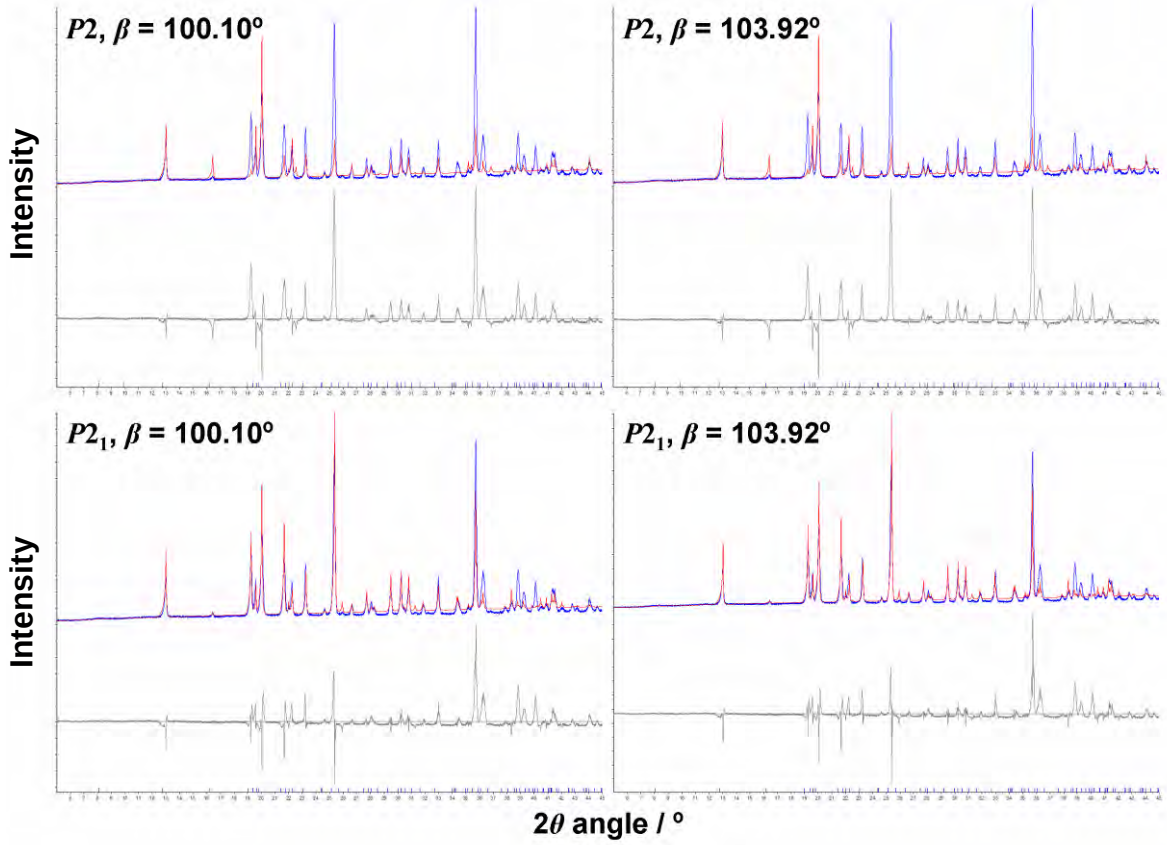

Figure 3-7. Difference (grey) powder X-ray diffraction spectra between the calculated (red) and experimental (blue) data for combinations of space groups and β-angles

Table 3-9. Values of R_{wp} (%), R_B (%) and GOF for the various space group and β-angle combinations

Space group	β-angle					
	100.10°			103.92°		
	R_{wp}	R_B	GOF	R_{wp}	R_B	GOF
$P2$	36.50	60.81	7.86	36.58	63.64	7.87
$P2_1$	25.72	51.28	5.54	26.32	50.92	5.65

As the lowest R_{wp} value obtained is still not acceptable at 25.72%, a re-refinement was done, including preferred orientation as a refinable parameter. This is justified by the fact that the sample was packed on the non-spinning Pt-heating strip using the top-loading technique, and thus during the thermal dehydration stage, the morphology of the sample can change (it is a platy material, new

crystallite formation/orientation, cracks in the powder surface, etc.) in such a way that preferred orientation is significantly present during measurement of the powder pattern. The preferred orientation was sufficiently modelled using an eight-order spherical harmonics function [17]. Table 3-10 displays the indices of agreement when preferred orientation is taken into account. Very importantly, during this second round of refinements the unit cell lengths and angles were also allowed to refine and the labels '100.1' and '103.92' for the β-angle serve only as labels from this point forward for comparison with Table 3-9.

Table 3-10. Values of R_{wp} (%), R_B (%) and GOF for the various space group and β-angle combinations with preferred orientation also refined

Space group	β-angle					
	100.10º			103.92º		
	R_{wp}	R_B	GOF	R_{wp}	R_B	GOF
$P2$	14.90	5.87	3.22	14.72	8.39	4.28
$P2_1$	11.10	3.40	2.39	13.37	4.88	2.88

All refinements dramatically improve the indices of agreement, but finally a single candidate can be identified as the most plausible solution to be optimised initially for the final refinement. The system was then again iteratively refined and the final structure solution using the rigid body was obtained as a = 5.407 Å, b = 10.387 Å, c = 12.887 Å and β = 100.071º in space group $P2_1$. Figure 3-8 shows the unit cell obtained for the final refinement; it can also be seen that the packing is chemically acceptable.

The final refinement, was done by removing the rigid body constraint and allowing all atoms to be able to move around independently from their original positions. When the final atomic positions were obtained, preferred orientation was introduced into the model for the last iteration of the final refinement. This was done as including preferred orientation initially in the final refinement could introduce systematic errors. The final structure obtained was still recognisable as HEDP, but slightly distorted. The difference XRD pattern between the experimental and calculated patterns is shown in Figure 3-9. The final indices of agreement were R_{wp} = 8.01%, R_B = 1.15% and GOF = 1.73.

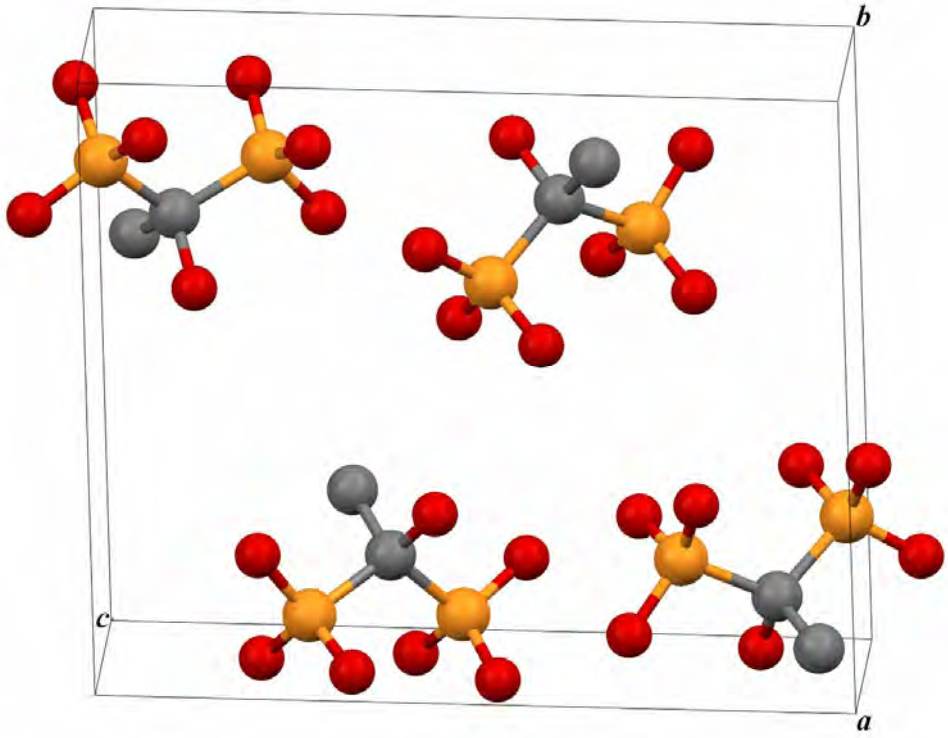

Figure 3-8. The unit cell packing obtained during the rigid body refinement for the unit cell $P2_1$ with β = 100.071°

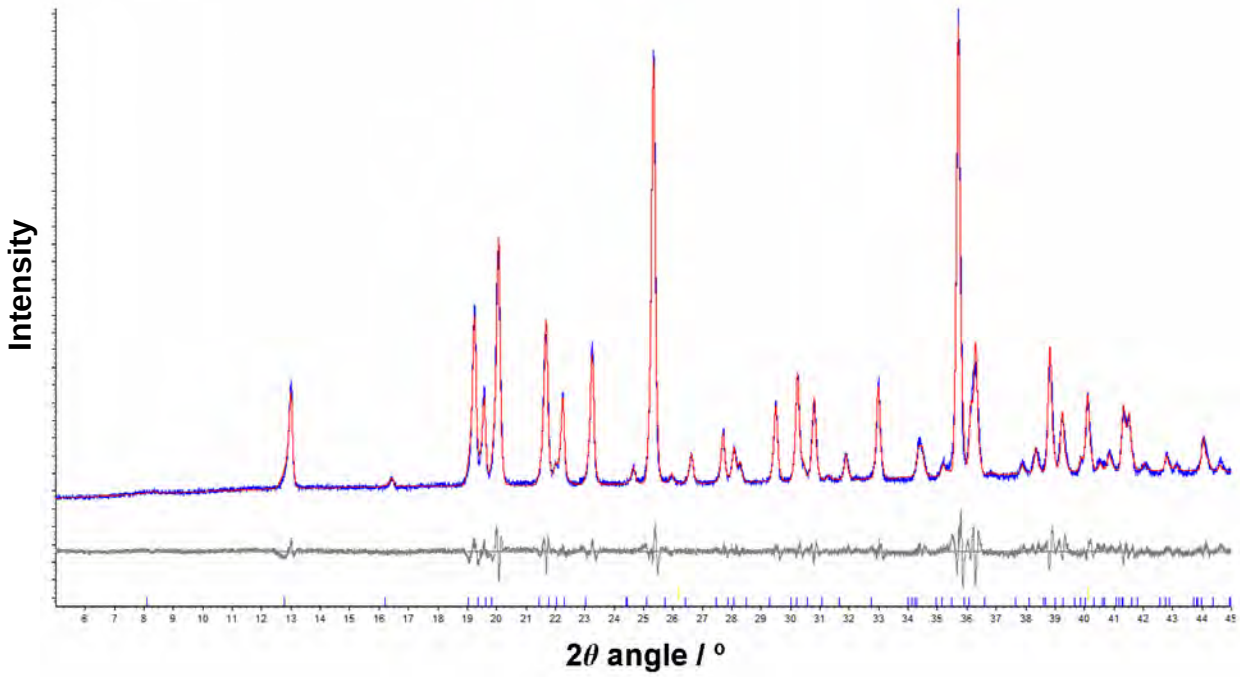

Figure 3-9. Difference (grey) powder X-ray diffraction spectra between the calculated (red) and experimental (blue) data for the final refinement of the structure

Figure 3-10 shows an overlay of the rigid body structure obtained with that finally obtained when the rigid body constraint was removed. The distorted nature required to model and obtain the best fit of the experimental powder pattern is highly probable due to the initial sampling methods. Data were not collected in a capillary set-up, which is ideally required to ensure that the intensity data are accurate. This facility was not available at the time the measurement was made. The data were collected on a Pt-heating strip: powder was placed on the strip and heated to the required temperature to remove the water of crystallisation and maintain the anhydrous form of HEDP during the measurement. During this dehydration process the powdered crystallites orientated themselves such that the preferred orientation of the crystallites contributed significantly to the intensity data, as seen from the comparison of the indices of agreement in Tables 3-9 and 3-10 before and after preferred orientation was included in the modelled system.

All these and other previously mentioned factors could also have contributed to the initial ambiguities of the cell parameters. This is also evidenced by the fact that one unit cell parameter became the most plausible solution after preferred orientation was taken into account. The positions of only the non-hydrogen atoms could be determined with a level of confidence. It would also have been advantageous to have been able to determine the hydrogen positions as this would have given more insight into the nature of hydrogen bonding for this molecule, specifically in the anhydrous solid state. Experimental determination of the hydrogen positions will definitely not be possible here as it is already difficult to determine them experimentally with good-quality X-ray data because twelve H atoms have approximately the same scattering contribution as one C atom. Ideally, to obtain hydrogen positions, high resolution neutron diffraction data of the deuterated analog could provide this answer.

Despite all the difficulties encountered, it seems that an acceptable determination of the crystal structure of anhydrous HEDP has been done. One aspect of the rigid body that was assumed, but that may not necessarily be true for anhydrous HEDP, is the orientation of the two PO_3H_2 moieties relative to each other. In HEDP·H_2O the PO_3 atoms of the two moieties, for all practical purposes, eclipse one another when one looks down the P1-P2 axis (Figure 3-11). From

the distorted structure obtained it would seem that this may not be the case as the two distorted PO_3 units seem to prefer a staggered conformation. In summary, Table 3-11 contains the X-ray crystallographic data as obtained from the Rietveld refinement for the rigid body structure, as well as the final distorted structure.

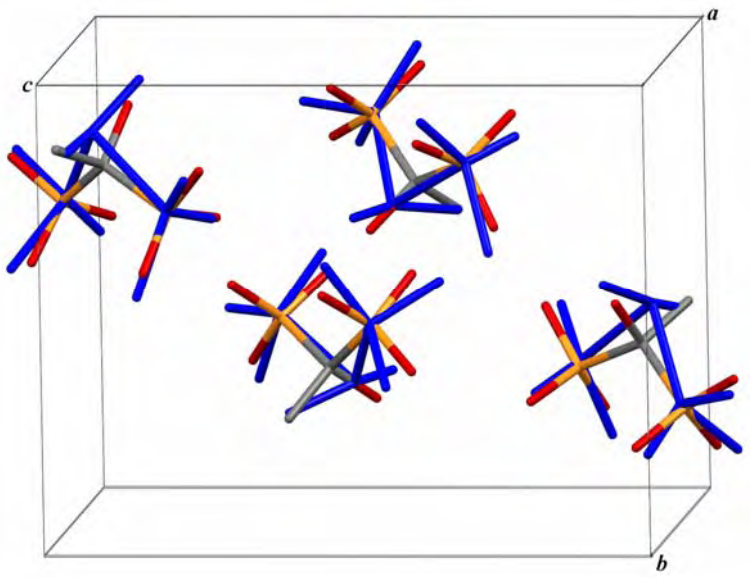

Figure 3-10. Unit cell packing of the rigid body structure superimposed on that of the atom-independent determined structure (blue)

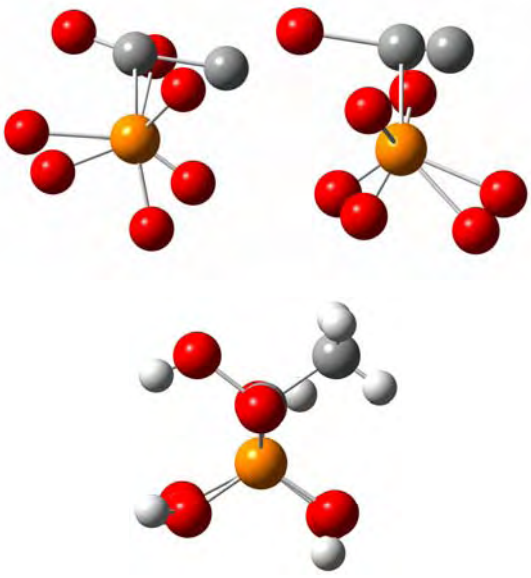

Figure 3-11. HEDP molecules viewed down the P1-P2 axis showing the two staggered (albeit distorted) H_4L units as determined by Rietveld refinement for the anhydrous case (top) compared with the eclipsed conformation in $HEDP{\cdot}H_2O$ (bottom)

Table 3-11. Crystallographic summary of the rigid body and independent atom determined structures of anhydrous HEDP

	Rigid body	Independent atom
Space group	$P2_1$	$P2_1$
a / Å	5.407	5.406
b / Å	10.387	10.285
c / Å	12.887	12.887
β / °	100.071	100.070
Z	2	2
R_{wp}	11.01%	8.01%
R_B	3.40%	1.15%
GOF	2.39%	1.73%

3.4.3 $CaH_2L{\cdot}2H_2O$

A first attempt at the single crystal structure determination for $CaH_2L{\cdot}2H_2O$ was done by Uchtman [18] but, similarly to $HEDP{\cdot}H_2O$, the hydrogen positions could not be experimentally determined. Since it was obvious from the literature [9] and during the structural investigation for anhydrous and monohydrated HEDP that hydrogen bonding plays such an important role in the chemistry and inter/intramolecular interaction of HEDP, a redetermination of the crystal structure was attempted and most of the hydrogen positions were successfully determined experimentally. Table 3-12 contains a summary of the crystallographic data as determined for the crystal structure. All other relevant data, bond lengths, bond angles and dihedral angles can be found in Table 1-B in the Appendix.

Figure 3-12A shows the molecular structure of $CaH_2L{\cdot}2H_2O$, as well as four other Ca-coordinated oxygen atoms. Similar to fully protonated HEDP, H_4L, the bisphosphonate molecule H_2L^{2-} can have C_s as its highest point group symmetry, but again adopts a C_1 conformation due to the hydrogen bonding stabilising the lattice. Calcium is eight-coordinated in this structure, with Ca-O bond lengths ranging between 2.3578(17) and 2.5921(18) Å (an average of 2.475 Å), which is

comparable to the average Ca-O bond length of 2.41 Å in calcium oxide at 298 K [19].

Table 3-12. Selected X-ray crystallographic data obtained for $CaH_2L \cdot 2H_2O$

Empirical formula	$C_2\ H_{10}\ Ca\ O_9\ P_2$	
Formula weight	280.12	
Crystal system	Triclinic	
Space group	$P\bar{1}$	
Unit cell dimensions	a = 6.9499(6) Å	α = 92.7330(10)º
	b = 7.5961(6) Å	β = 106.3140(10)º
	c = 9.7000(8) Å	γ = 112.4250(10)º
Volume	447.33(6) Å^3	
Z	2	
Density (calculated)	2.080 g.cm^{-3}	
Final R indices ($I > 2\sigma(I)$)	R_1 = 0.0339, R_{w2} = 0.0942	
R indices (all data)	R_1 = 0.0344, R_{w2} = 0.0947	

Parallel to the ab-face of the unit cell, a network of infinite two-dimensional layers is formed, and each layer is linked via bridging coordination of the Ca atoms with the O8 atom of the water molecules, as well as the H_2L^{2-} molecular unit; other extensive intermolecular hydrogen bonding also occurs. Two symmetry-related H_2L^{2-} units bridge pairs of Ca atoms, with each Ca atom forming a six-membered chelate ring by bonding through the O1 and O4 oxygen atoms of one of the H_2L^{2-} units, and forming a five-membered ring with the other H_2L^{2-} unit by bonding with its O2 and O7 oxygen atoms. The Ca···Ca pair distance is 5.4237(10) Å. Two four-membered rings, $(Ca1\text{-}O2)_2$ and $(Ca1\text{-}O8)_2$, are also formed when two symmetry-related O2 H_2L^{2-} atoms and two symmetry-related O8 water oxygen atoms form coordination bridges to other Ca atoms, resulting in Ca···Ca distances of 3.7907(9) Å and 4.1334(9) Å for the O2- and O8-four-membered rings respectively. This results in each Ca atom being linked by coordination bridges to three other Ca atoms, forming the previously mentioned infinite

two-dimensional network layers. All these rings discussed are shown for clarity in Figure 3-12B. At this point it should be noted that the proton on O6 is equally disordered between O5 and O6, and these network layers are linked via hydrogen bonds between O5-H5···O5*, O6-H6···O6** and O9-H9$_b$···O6$^{\#\#}$, where the symmetry transformations are *: $-x + 1, -y + 1, z$, **: $-z + 1, -x + 1, -y + 2, -z + 1$ and ##: $x, y, z - 1$ respectively. Due to the disorder of the O6 proton, it is presumed that one hydrogen bond is formed for each O$_n$-H$_n$ (n = 5, 6) link, where one O atom is protonated (acting as the donor) and the other unprotonated (acting as the acceptor).

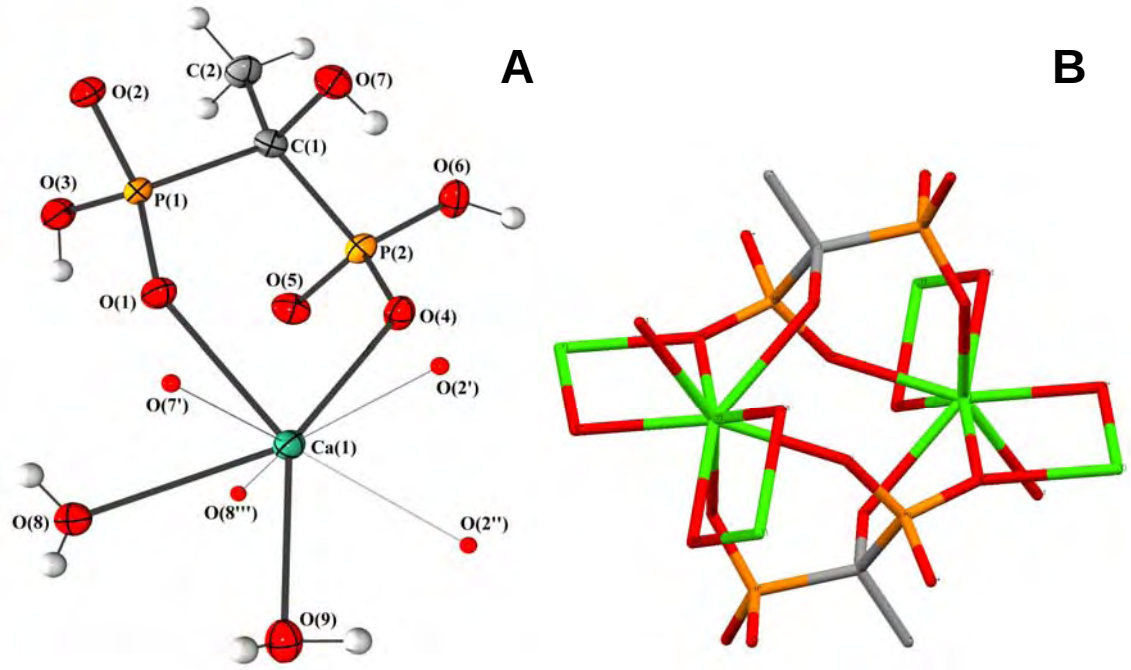

Figure 3-12. A. An Ortep/POV-ray drawing of the molecular unit of $CaH_2L{\cdot}2H_2O$ showing the eight-coordinate nature of the calcium atom. Ellipsoids are shown at the 50% probability level and the symmetry transformations used to generate the equivalent positions are ': $-x, -y + 1, -z$; '': $x + 1, y, z$; ''': $-x + 1, -y + 2, -z$ B. Capped stick representation of the partial crystal structure of $CaH_2L{\cdot}2H_2O$ showing the four, five and six membered formed in the crystal structure as discussed in the text.

3.5 Vibrational spectroscopy and molecular modelling

3.5.1 HEDP and its various protonated forms

3.5.1.1 Solid-state spectroscopy

As already discussed, HEDP has both a monohydrate and anhydrous phase in the solid state, and also has the various protonated forms, H_4L, H_3L^-, H_2L^{2-}, HL^{3-} and L^{4-}, that exist in an aqueous solution. Vibrational spectroscopy (and specifically Raman spectroscopy because of its versatility) is an ideal tool for investigating the structural changes that occur during the loss of hydration and solvation under different conditions. Figure 3-13 shows the Raman spectra of HEDP·H_2O and HEDP for the region 100 – 1600 cm^{-1} and Figure 3-14 shows the Raman spectra for the two compounds for the region 2600 – 3200 cm^{-1}. Due to the structural rearrangement, the most prominent changes in the Raman spectrum occur predominantly in the vibrational bands associated with the PO_3H_2 moieties and that associated with the water of hydration. Vibrational band assignments can be found in Table 3-13. Various sources (references [20-25]) were used to make the complete empirical assignment for HEDP·H_2O. Assignments for anhydrous HEDP were tentatively confirmed and refined by means of molecular modelling of a single H_4L unit conformer. Generation of this modelled conformer is discussed in more detail later on in this chapter under Section 3.5.1.2.

In the low wavenumber region, seen in Figure 3-13, the most notable changes are the appearance of a lattice mode at 168 cm^{-1} and the disappearance of the hydrogen bond band at 241 cm^{-1}. A weak band at 233 cm^{-1} in the spectrum of anhydrous HEDP is assigned to a similar hydrogen bond band, but should occur either inter- or intramolecularly between to H_4L units as this type of bonding was observed in both the $H_4L·H_2O$ and $CaH_2L·2H_2O$ cases . The band at 274 cm^{-1} of HEDP·H_2O is assigned to the ρPO-H / δC-C-O band as it seems that this band could be affected by a loss of hydration and is therefore not observed in the anhydrous HEDP spectrum. In general, bands will shift to a higher wavenumber

(if otherwise not dramatically affected by structural factors) as temperature increases. The shift of the ρPO-H band from 343 cm^{-1} to 327 cm^{-1} is indicative of structural change as the band shifts to a lower value rather than a higher one. The changes and 'simplification' of the band structure for the region 411 – 528 cm^{-1} are attributed specifically to the loss of hydration as all these bands are associated with the PO_3H_2 or COH groups. The ν^sC-P band at 627 cm^{-1} shifts to 632 cm^{-1} and does not seem to be affected by the structural rearrangement. It is known that this vibration is very likely to be mixed up with other vibrations [20] and it is also far removed from sites affected by the loss of hydration. The νC-CO band at 822 cm^{-1}, however, shifts lower and is also lower in intensity for anhydrous HEDP than HEDP·H_2O, and thus indicative of the rearrangement occurring during the dehydration process.

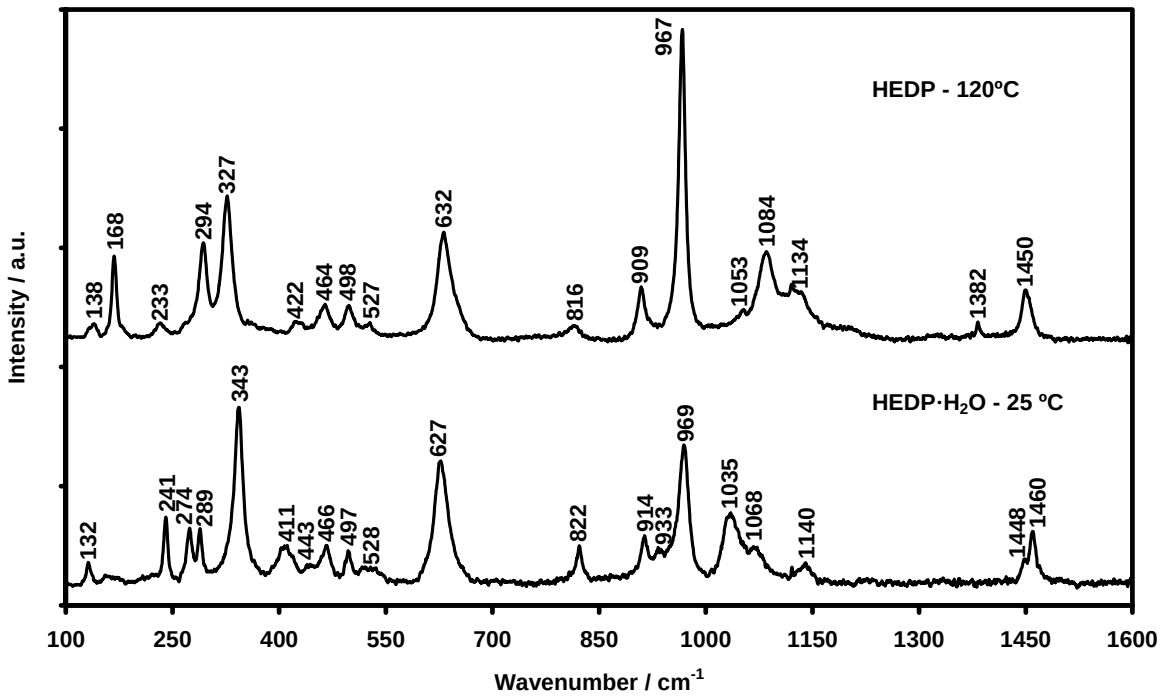

Figure 3-13. Raman spectra of HEDP·H_2O and anhydrous HEDP showing the bands mostly associated with vibrational bands involving non-hydrogen atoms

The bands found between 933 and 1140 cm^{-1} are assigned to stretching vibrations involving specifically the PO_3H_2 groups. Compounds containing P=O and P-OH groups have complex band structures in this region, making analysis

difficult [20]. Despite this limitation, it can still be seen that changes in relative intensities and band positions are indicative of the structural change. There is a notable increase in intensity of the strongest band at 969/967 cm^{-1}, assigned to the ν^{s}P-O(H) band, as the two PO_3H_2 moieties become chemically equivalent (but not necessarily symmetry equivalent) as water of hydration is lost. The well-described [20] δ^{as}C-CH_3 bands at 1448, 1460 and 1450 cm^{-1} are observed in both spectra, but in the anhydrous case the weak band at 1382 cm^{-1}, assigned to the δ^{s}C-CH_3, becomes Raman active and is a good indicator of the presence of a CCH_3 moiety [20].

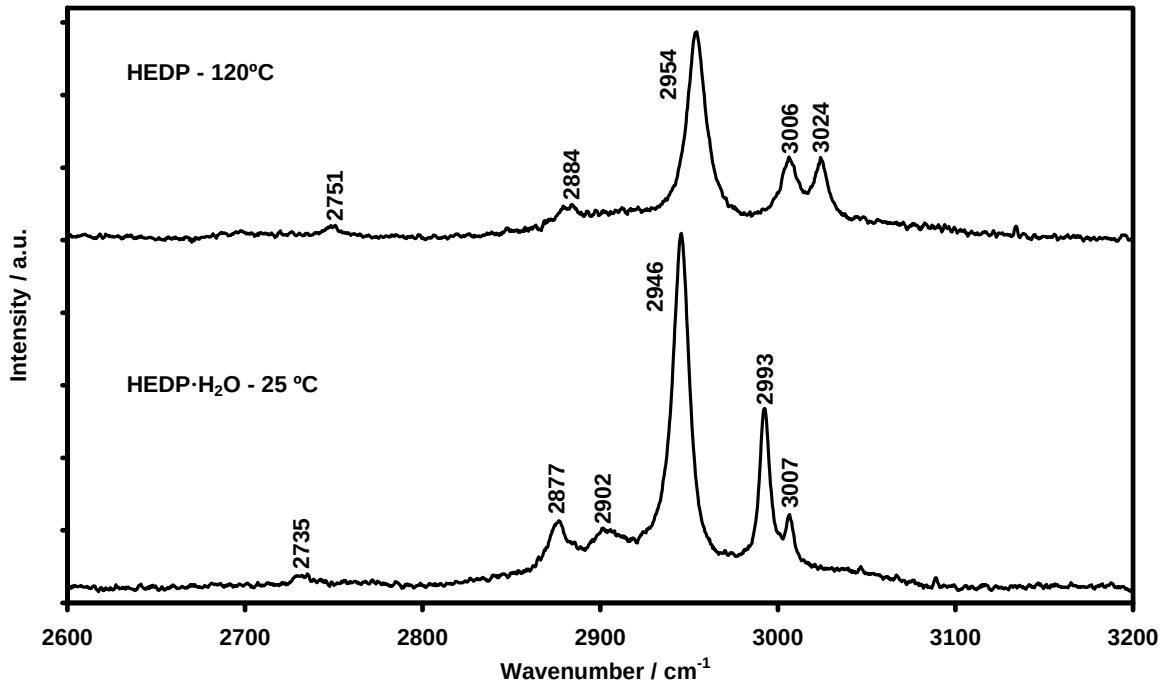

Figure 3-14. Raman spectra of HEDP·H_2O and anhydrous HEDP of the spectral region associated with the CH_3 and OH stretching bands

Only two notable differences are observed in the νCH/OH region of the Raman spectra. The band at 2902 cm^{-1}, assigned to the hydrogen-bonded νOH vibration, is not present in the anhydrous HEDP spectrum and the relative intensity of the two $\nu^{as}CH_3$ bands at 2993 and 3007 cm^{-1} change as one goes from the HEDP·H_2O to anhydrous HEDP, also probably due to structural effects.

Figure 3-15 shows the mid-infrared spectrum for HEDP·H_2O and anhydrous HEDP for the region 400 – 4000 cm^{-1}, and their assignments can be found in

Table 3-13. Similar rationales can be employed to explain changes in the vibrational bands observed, and only the most important spectral features will be discussed. Bands associated with the δOPO vibrations (<550 cm^{-1}) are observed to be more intense in the IR spectrum than in the Raman spectrum for both compounds, while the stretching vibrational bands associated with the PO_3H_2 moieties show a complex and overlapping band structure in the 900 – 1300 cm^{-1} region relative to the more well-defined, albeit still complex, structure of the same region in the Raman spectrum. The water-associated bands of HEDP·H_2O are broad and strong in intensity and, in conjunction with the broad bands usually associated with phosphonic acids [20], make analysis of the high-wavenumber region difficult. Bands indicated with an * in Figure 3-15 at 697, 1649, 3285 and 3483 cm^{-1} are assigned to the water of hydration [21, 25].

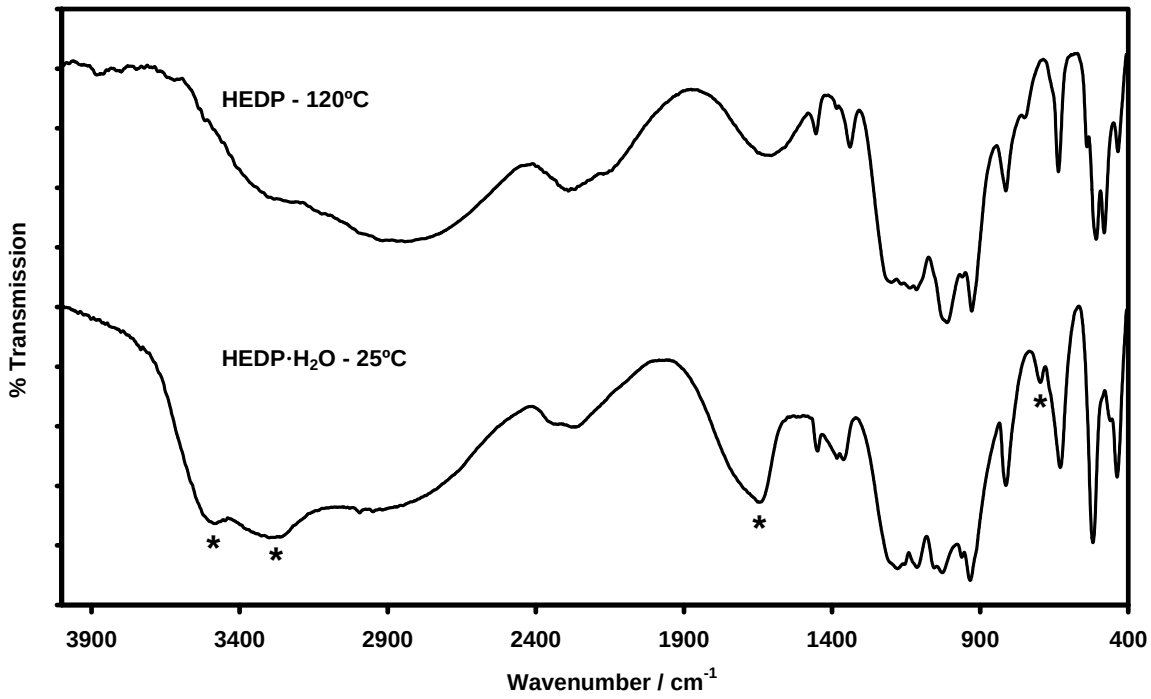

Figure 3-15. Mid-infrared spectrum of HEDP·H_2O and anhydrous HEDP prominently showing the bands associated with H_2O (marked *) disappearing during the loss of hydration

Table 3-13. The vibrational assignment of HEDP·H_2O and anhydrous HEDP

Assignment	HEDP·H_2O		HEDP	
	Infrared	Raman	Infrared	Raman
Lattice		132 w		138 w
Vibrations				168 m
Inter or intraHEDP				233 w
νOH···O				
νOH···OH_2		241 m		
ρPO-H / δCCO		274 m		
δC-C		289 m		294 m
ρPO-H		343 vs		327 s
ρCO-H		411 w		422 w
	438 m	443 w	435 m	
ρPO-H	461 w, sh	466 w		464 w
		497 w	481 s	498 w
	520 s	528 w	508 s	527 w
			540 m, sh	
ν^sC-P	620 m	627 s	636 m	632 s
H_2O libration	697 w			
-			750 m, sh	
νC-CO	813 m	822 w	813 m	816 vw
νC-O-H		914 w		909 w
ν^sP-O(H)	933 vs	933 w	929 vs	
	962 vs	969 s	960 s, sh	967 vs
			1011 vs	
	1028 vs		1023 vs, sh	
δPO-H / ν^{as}P-O(H)		1035 m		
				1053 vw, sh
	1055 vs, sh			
		1068 w		1084 m
	1114 vs		1115 s	
νP=O / δPOH		1140 vw	1137 s	1134 w, sh
	1155 vs, sh			
			1166 s, sh	
	1178 vs			
	1202 vs, sh		1200 s	
-	1362 m		1339 w	
δ^sC-CH_3	1384 m		1385 w, sh	1382 vw
δ^{as}C-CH_3	1449 m	1448 w,sh	1454 w	1450 w
		1460 m		
νO=P-OH			1607 m, br	
δH_2O	1649 s, br			
νO=P-OH			2171 m, sh	
	2279 m, br			
			2290 s, br	
	2328 m, sh			
νPO-H		2735 vw		2751 vw
νO=P-OH	2830 s, br		2842 s, br	
$\nu^s CH_3$		2877 m		2884 m

Assignment	HEDP·H_2O		HEDP	
	Infrared	Raman	Infrared	Raman
νOH_2		2902 m		
$\nu^{s}CH_3$	2950 w	2946 vs		2954 vs
$\nu^{as}CH_3$	2995 w	2993 s		3006 s
		3007 m		3024 m
νOH_2	3285 vs, br			
	3483 vs, br			

ν: stretch, δ: deformation, ρ: rock
s: symmetrical, as: anti-symmetrical
vw: very weak, w: weak, m: medium, s: strong, vs: very strong
sh: shoulder, br: broad

Interestingly, it has been noted that the relative intensities of the broad bands centred at approximately 2800, 2300 and 1600 cm^{-1} can be used to distinguish between $RP{=}O(OH)_2$ and $R_2P{=}O(OH)$ acids [20]. In the IR spectrum of compounds containing the $P{=}O(OH)_2$ moieties, the 1600 cm^{-1} band has the weakest intensity of the three bands, whereas it is the strongest band in compounds containing the $R_2P{=}O(OH)$ acid functionality. Comparison of the three bands' intensities in the IR spectrum obtained for anhydrous HEDP shows that the 1600 cm^{-1} band is of lowest intensity as is expected for HEDP which can be classified as being an $RP{=}O(OH)_2$ acid, indicating that no thermal degradation has occurred regarding the two PO_3H_2 moieties.

3.5.1.2 Solution spectroscopy

HEDP solutions in aqueous medium were investigated by means of Raman spectroscopy as it is by far the superior vibrational technique when investigating systems of an aqueous nature. The degree of protonation of HEDP is highly pH-dependent [7] and thus knowledge of the solution's pH indicates what species are present or vice versa. In Section 3.2 it was shown that this change can be followed by means of NMR spectroscopy, but NMR spectroscopy could not differentiate between the presences of discrete species in this case as the two techniques measure very different molecular properties. Figure 3-16 shows the experimental species distribution diagram obtained from the experimental pK_a values of HEDP [5] for the pH range 0.98 – 13.00. It can be seen that the

distribution is relatively uncomplicated, except in the region for H_3L^- where both H_4L and H_2L^{2-} overlap simultaneously.

Analysis of the FT-Raman spectra over the measured range of 100 – 3500 cm^{-1} showed that observable spectral changes occurred only in the region 860 – 1280 cm^{-1}, which contains the bands associated with the PO_3H_2 moieties. This is rationalised by the change in PO bond order that occurs as deprotonation progresses. Figure 3-17 shows a topographical plot of the 860 – 1280 cm^{-1} wavenumber region for pH = 0.98 – 13.00; the bands assigned to each protonated form of HEDP are indicated. The dominant PO bands at 957, 1061, 968 and 989 cm^{-1} can be assigned to the H_4L/H_3L^-, H_2L^{2-}, HL^{3-}, and L^{4-} species respectively. At low pH, the broad band observed at 1186 cm^{-1} is assigned to a mixed intra/intermolecular POH/water hydrogen-bonded band. Other bands observed in the Raman spectra during the investigation are at ~640, 1450, ~2878 and 2937 cm^{-1}, and are assigned to the ν^{s}C-P, $\delta^{as}CH_3$, $\nu^{s}CH_3$ and $\nu^{as}CH_3$ vibrations respectively [18]. It should be noted that over the whole measured pH range, the position of the ν^{s}C-P gradually shifted from 635 to 644 cm^{-1}. This shift to a higher wavenumber value as a function of pH has been reported previously [24].

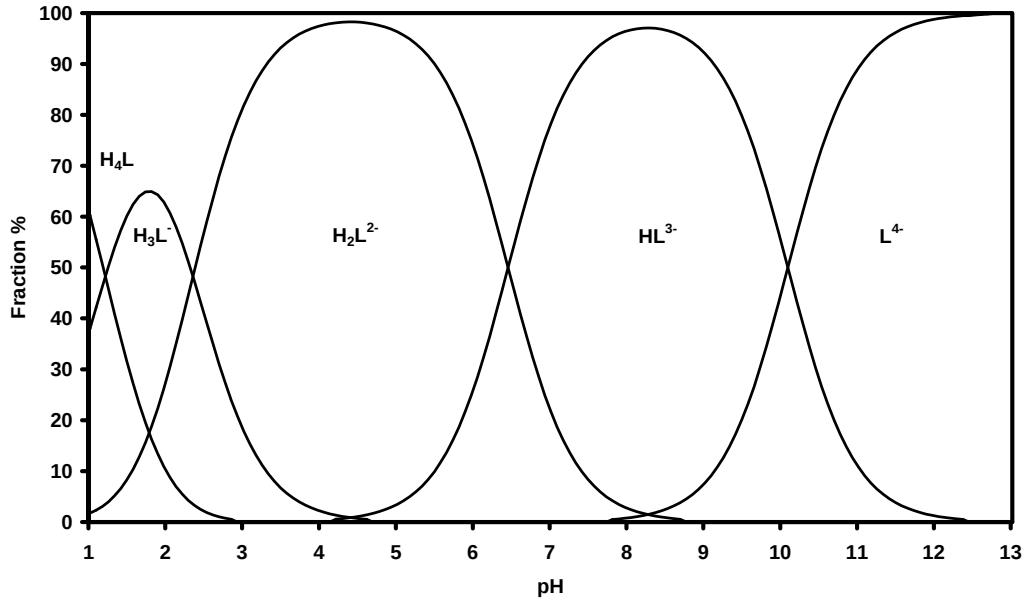

Figure 3-16. The species distribution diagram of HEDP(aq) for the pH region 0.98 – 13

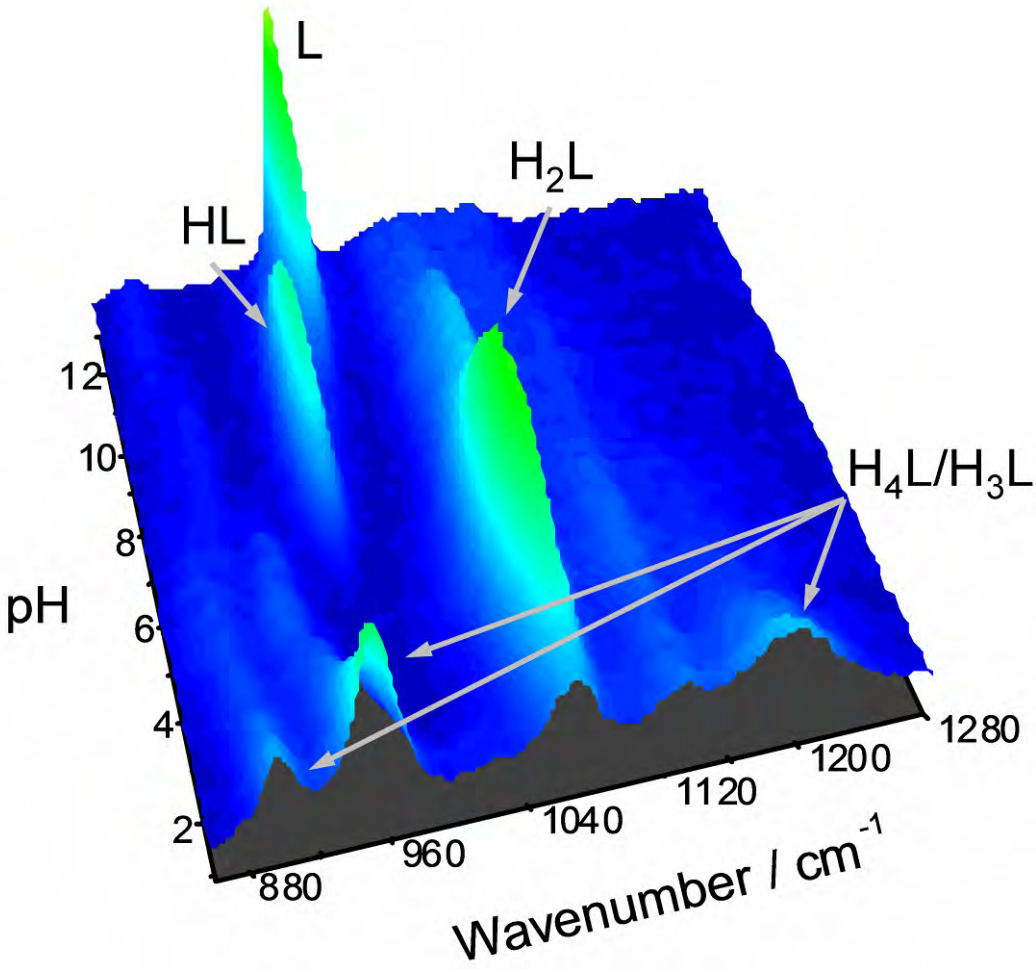

Figure 3-17. Topographical plot of the 860 – 1280 cm^{-1} wavenumber region for pH = 0.98 – 13.00 showing the bands of the various pH-dependent protonated forms of HEDP as indicated

It can be seen from Figure 3-16 that Raman spectroscopy does allow the discrete observation of the various protonated species of HEDP. Even though NMR could not differentiate between discrete species, it is seen in Figure 3-18 that if we define x as the independent variable for the function plotted in Figure 3-1, it accurately follows the same trend as the appearance and disappearance of the νPO Raman bands of the various protonated forms of HEDP where the ^{31}P NMR data are superimposed on a stack plot of the Raman spectra of the νPO region for the pH range 0.98 – 13.00.

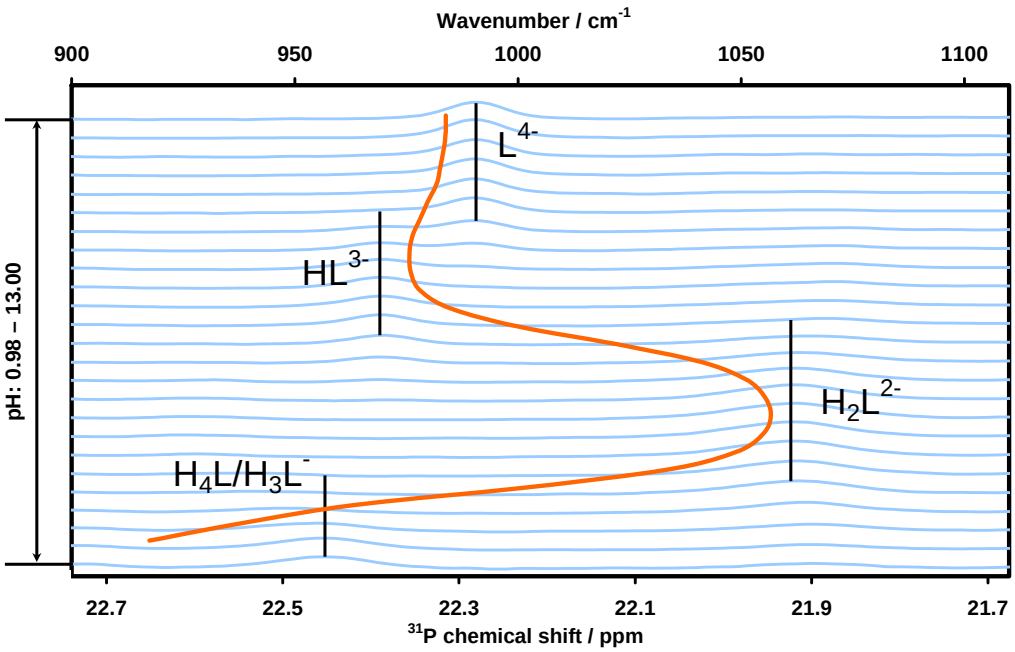

Figure 3-18. An overlay plot showing the similar trend of the ^{31}P NMR chemical shift relative to the discrete Raman band positions of the various protonated forms of HEDP for the *ν*PO vibrational region

Even in solution, HEDP produces a complex Raman spectrum for analysis in the *ν*PO region, which fortunately simplifies as HEDP is deprotonated at higher pH values. Various attempts at modelling the vibrational spectrum of HEDP·H_2O in the solid state did not reproduce the experimental vibrational spectrum satisfactorily. This is most probably due to the strong contribution of the hydrogen-bonded water molecule, as well as to the infinite hydrogen-bond networks that exist in the solid-state crystal structure. In solution, the HEDP molecule is free of solid-state interferences and constraints, and the Raman spectrum is simplified due to the dynamic nature of solutions. Unfortunately, due to the free bond rotation that occurs in solution for HEDP, the problem arises of determining which conformer for each species is the most probable to model and reproduce correctly the experimentally observed spectrum as the theoretical calculation is done on a statically solvated molecule and HEDP itself is not rigid. The strong hydrogen bond present in the solid-state structure indicates that strong inter- and intramolecular interaction should not be ignored in solution as it has previously been reported that this is highly likely to occur at low pH and high HEDP concentrations [24]. Taking all these factors into account, it is therefore

highly probable that there is a strong preference (energetically or sterically) for certain conformers to be predominant in solution. In Figure 3-19 it can be seen that both H_4L and L^{4-} are achiral, with L^{4-} having the highest degree of rigidity of all the protonated forms. H_3L^- and HL^{3-} are chiral, due to the non-equivalent degree of protonation for the two PO_3H_2 moieties but, in principle, H_2L^{2-} could be either chiral (both H^+ on the same phosphonic group) or achiral (one H^+ per phosphonic group). The chiral form of H_2L^{2-} was disregarded in this case. Judging from the similarity in pK_a values of H_4L and H_3L^- (Table 3-3), as well as from the crystal structures known for metal complexes containing H_2L^{2-} [9], the successive deprotonation will not occur from only one phosphonic acid group, but will rather involve one H^+ from each phosphonic group. All conformers that were either non-convergent or generated imaginary (i) wavenumbers were deemed unsuitable for further analysis, as they are not at an energy minimum for the molecule. There is no experimental evidence that the COH proton is removed; this aspect was not investigated.

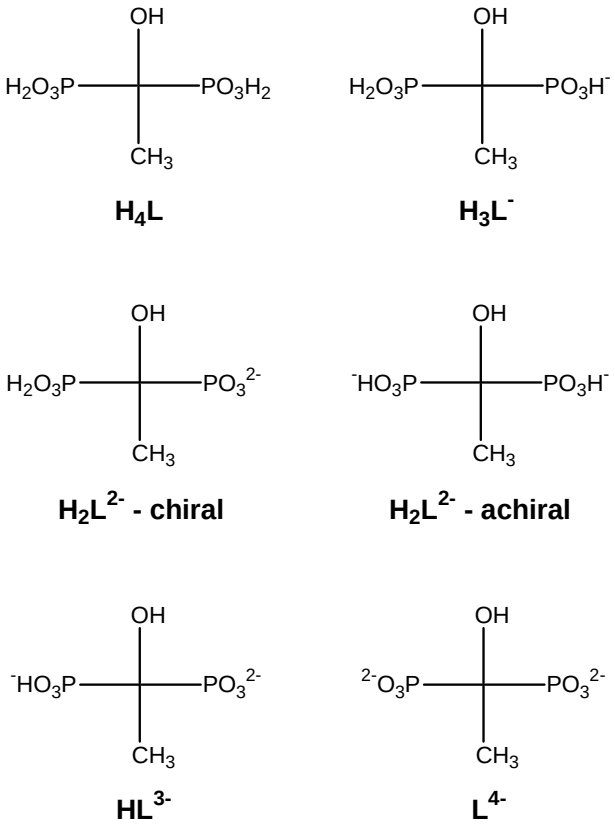

Figure 3-19. The various degrees of protonation possible for HEDP in solution

The conformational analysis done was by no means complete, but only preliminary to see if sensible conformers could be obtained to verify and explain the measured solutuion Raman spectra for the various protonated forms of HEDP(aq). H_4L proved to be the most problematic of all the protonated forms as it is not a rigid molecular system. As quantum mechanical calculations are time-consuming, the simpler molecular mechanics approach was employed first to generate initial starting conformers for H_4L. The Macromodel software package generated 31 non-equivalent, convergent conformers for H_4L, after a 1000 cycle molecular dynamics run. These 31 conformers had an energy distribution of 20.4 kJ/mol from the lowest to the highest energy conformer generated. At this point it should be mentioned that energies calculated by molecular mechanics have no physical meaning, but can still be used on a preliminary level to distinguish conformeric candidates that would have the lowest energy relative to other conformers. Fifteen of the conformers' mirror images were also determined and only one contained an internal mirror plane, accounting for all 31. The two conformers of lowest single-point energy contribute 21.3% to the total conformer population, and each contains two intramolecular hydrogen bonds. On this basis, these two conformers were further used for DFT calculations. Both conformers generated an *i*-wavenumber in their DFT-calculated vibrational spectra after being DFT-optimised first, indicating saddle point structures. These Raman spectra also do not compare satisfactorily with the experimental data as the experimental Raman spectra do not contain contributions from only H_4L (H_3L^- is present in significant quantities as seen from the species distribution diagram, Figure 3-16) and experimentally there seems to be strong intra/intermolecular hydrogen-bond influences as well. Figure 3-20 shows all 31 of the convergent conformers generated with the Macromodel software for H_4L, with the corresponding C and P atoms superimposed on each other. The CH_3 moiety is rigid for all conformers and the COH moiety can be seen to have only three main orientation possibilities ~120º from one another. The spread of orientations of the PO_3H_2 is a good indication of the difficulties encountered for H_4L and therefore molecular modelling of the H_4L Raman spectrum could not assist in the identification of a predominant conformer or the assignment of the Raman bands of H_4L. A full, extensive conformational analysis of H_4L would therefore be required to find the true energy minimum structure.

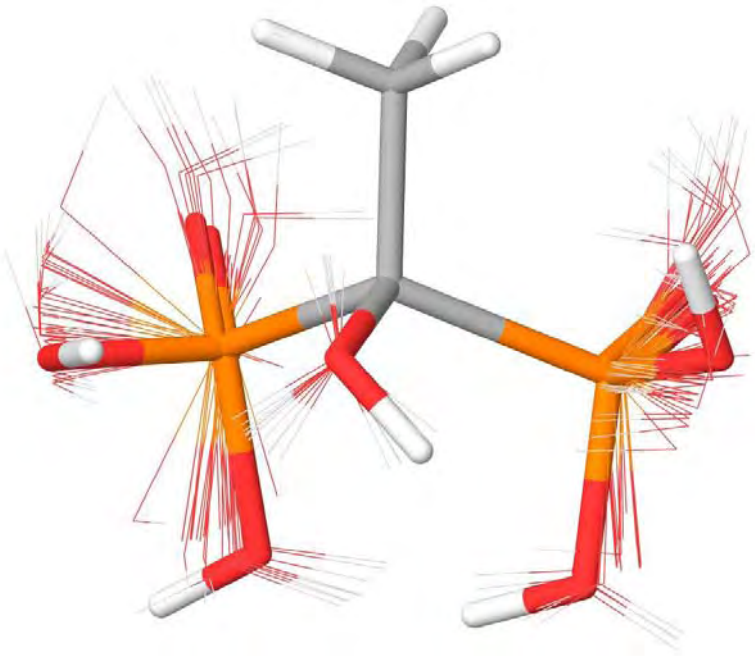

Figure 3-20. Superimposed structures of the 31 converging MM theory generated H_4L conformers. The conformer of lowest relative energy is illustrated as the tube structure

Curiously, by comparison, the theoretical Raman spectrum of the lowest energy conformer matched that of the experimental solid-state Raman spectrum of anhydrous HEDP (H_4L), and was used to tentatively confirm assignments as mentioned in Section 3.5.1.1. The assignment of the Raman spectrum of H_3L^- caused similar problems, but at least a most probable conformer could be determined. These difficulties are all ascribed to the hydrogen-bond interactions that are expected in this pH and concentration region [24]. All valid conformers found for H_3L^-, H_2L^{2-}, HL^{3-} and L^{4-} can be seen in Figure 3-21.

Vibrational assignments in the Raman spectra below 600 cm^{-1} were made difficult by the presence of a broad band centred at 479 cm^{-1} originating from the glass of the NMR tubes, as well as by the significant baseline fluorescence that was observed at lower wavenumbers for all samples. The vibrational assignments for H_2L^{2-}, HL^{3-} and L^{4-} above 600 cm^{-1} can be found in Table 3-14. A scale factor of 1.052 was used, except for bands marked with an *, which are reported unscaled.

This scale factor was calculated by comparing the experimental data with the theoretical data, and using the $\nu^{S}PO_3$ as reference point.

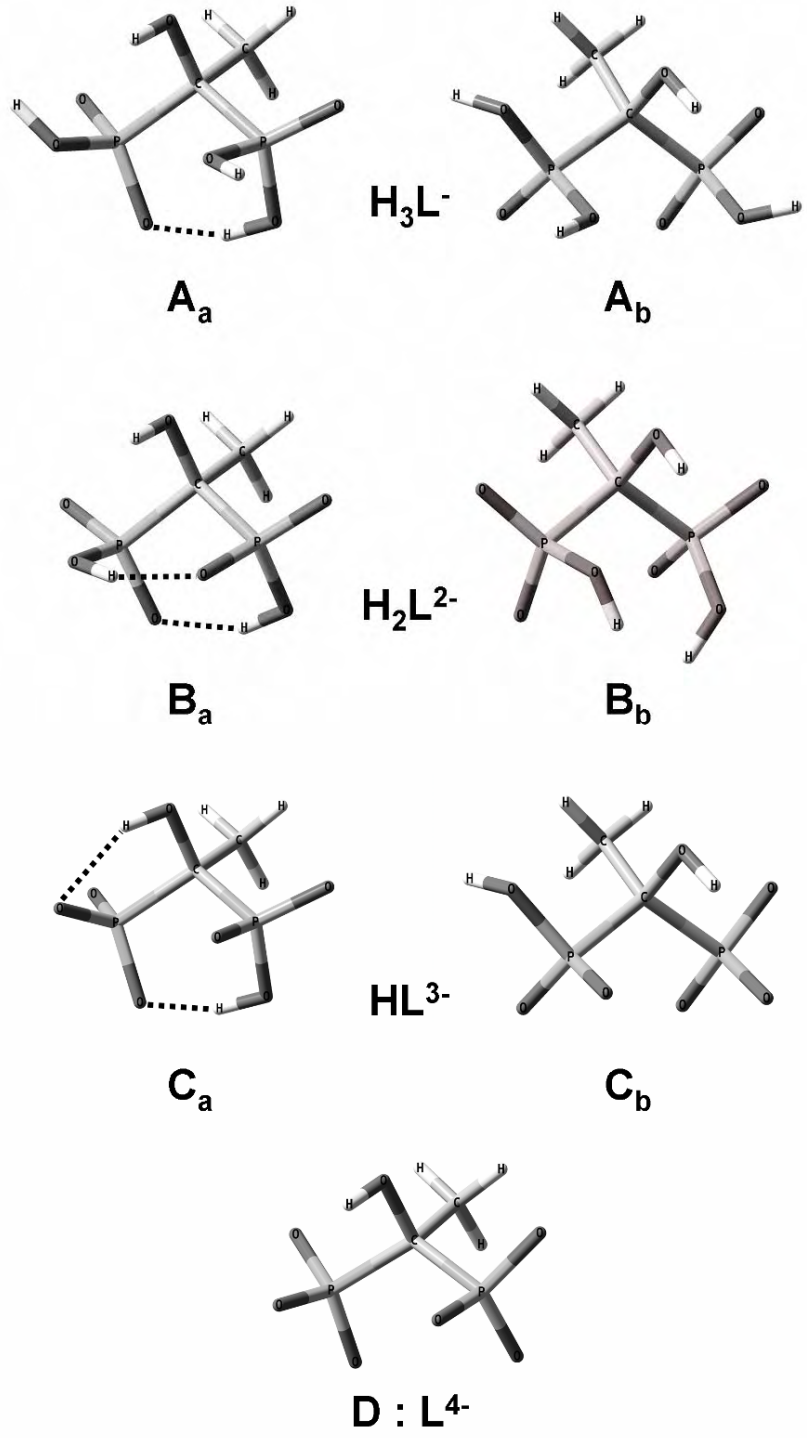

Figure 3-21. All conformers that did not give *i*-wavenumbers during the vibrational analysis for A: H_3L^-, B: H_2L^{2-}, C: HL^{3-} and D: L^{4-}. The intramolecular hydrogen-bonded conformers (a) were preferred above the (b) non-hydrogen-bonded conformers

Table 3-14. Vibrational assignment for the Raman spectra of the H_2L^{2-}, HL^{3-} and L^{4-} protonated forms

Assignment [20]	H_2L^{2-}		HL^{3-}		L^{4-}	
	Exp.	Calc.	Exp.	Calc.	Exp.	Calc.
ν^{s}C-P	637 m	634	639 m	638	645 w	634
νC-CO	808 vw	833	797 w	795	808 vw	799
νC-OH	926 vw	967	899 w	942	885 vw	903
$\nu^{s}PO_3^{2-}$	-		970 s	972	989 vs	992
$\nu^{s}PO_3^{-}$	1061 s	1071	-		-	
$\nu^{s}PO_3^{-}$ / $\nu^{as}PO_3^{2-}$	-		1069 m	1081	-	
νPO / νC-C / δCC-O	1132 w,br		1132 w,br		1105 w,br	
$\delta^{s}CH_3$	1381 vw	1402	1377 vw	1390 1400	1367 vw	1382
$\delta^{as}CH_3$	1454 w	1555 1563	1454 w	1550 1557	1452 vw	1555
$\nu^{s}CH_3^{*}$	2878 w	3031	2880 w	3027	2875 w	3025
$\nu^{as}CH_3^{*}$	2939 m	3097 3117	2937 m	3095 3104	2937 m	3094 3102
νPO-H*	2995 w	2910	2995 w	2907	-	

ν: stretch, δ: deformation
s: symmetrical, as: anti-symmetrical
vw: very weak, w: weak, m: medium, s: strong, vs: very strong
sh: shoulder, br: broad
* unscaled

Figure 3-22 shows the experimental Raman spectrum of a solution at pH 4.40 where H_2L^{2-} is present at maximum concentration, as well as those of two calculated conformers of two H_2L^{2-} that gave no *i*-wavenumbers for the region 600 – 1800 cm^{-1}. From calculation it was found that the broad band centred at ~1131 cm^{-1} represents vibrations associated with νPO, νC-C and δCC-O modes or mixtures thereof. The $\nu^{s}PO_3^{-}$ at 1061 cm^{-1} and the ν^{s}C-P at 637 cm^{-1} are the most intense bands in the experimental Raman spectrum of H_2L^{2-} and correlate best with the calculated Raman spectrum of conformer B_a. Conformer B_a has two intramolecular hydrogen bonds of ~1.8 Å each. A band observed at 2995 cm^{-1}, assigned to νPOH, is strongly indicative of intramolecular hydrogen bonding as it has been reported that this type of hydrogen bond can shift the νOH band to as low as 2500 cm^{-1} [20]. A shift to a lower wavenumber value of this band (due to the intramolecular hydrogen bonding) was also observed in the theoretical spectrum. In addition, the energy of conformer B_a has been calculated to be

30.84 kJ/mol lower than that of conformer B_b, making B_a the thermodynamically favoured conformer.

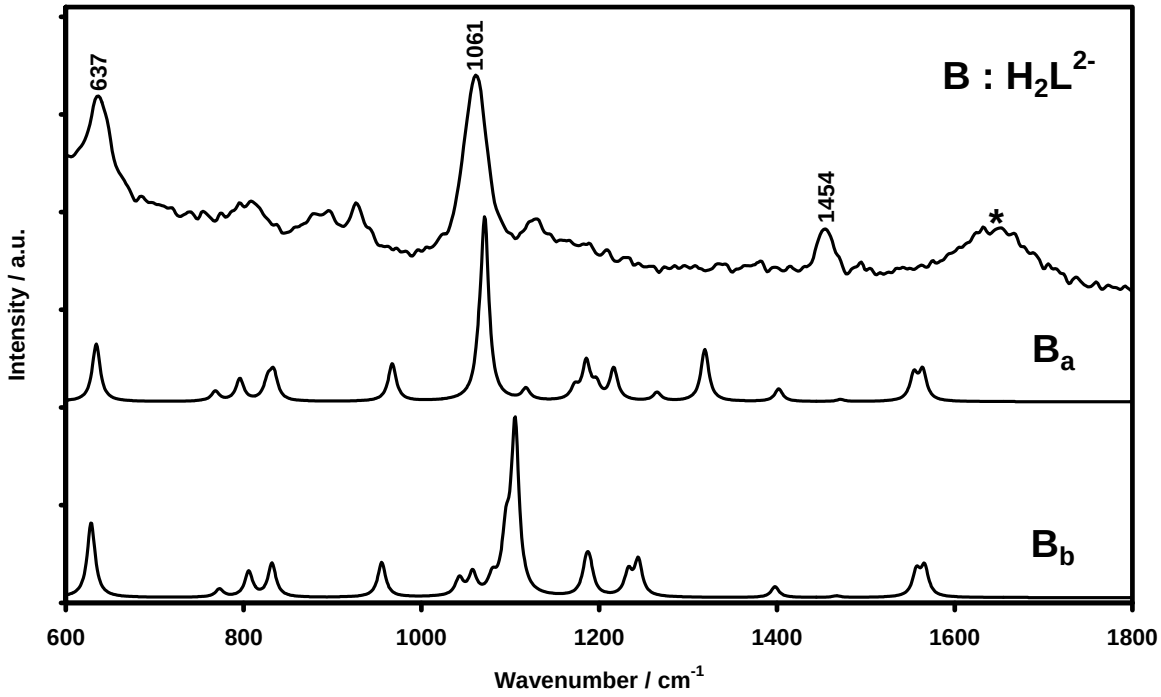

Figure 3-22. Comparison between the experimental and theoretically calculated Raman spectra for H_2L^{2-}. The band marked with an * originates from the solvent water

Figure 3-23 shows the experimental Raman spectrum of a solution at pH 8.20 where HL^{3-} is present at maximum concentration, as well as that of two calculated conformers of HL^{3-} that gave no *i*-wavenumbers. Once again, the broad band centred at ~1132 cm^{-1} represents vibrations associated with the νPO, νC-C and δC-C-O modes or mixtures thereof. The two calculated spectra look similar but, on closer inspection, the spectrum of conformer C_a matches the experimental data better, especially for the 637, 797, and 970 cm^{-1} bands. In addition, the calculated energy of conformer C_a was found to be 26.5 kJ/mol lower than that of conformer C_b, suggesting that it is thermodynamically more favoured, probably due to the two calculated intramolecular hydrogen bonds of 1.6 and 2.1 Å which exist at the POH···OP' and COH···OP' moieties. Once again a band at 2995 cm^{-1} is observed, which is indicative of the presence of intramolecular hydrogen bonding as found in conformer C_a.

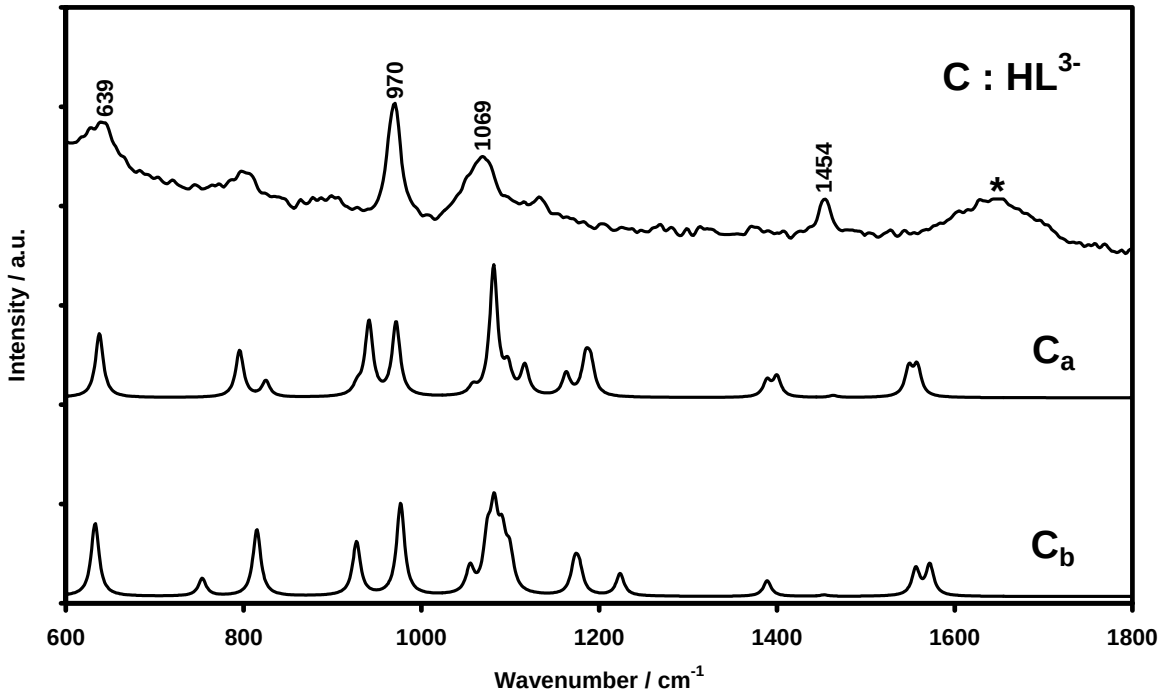

Figure 3-23. Comparison between the experimental and theoretically calculated Raman spectra for HL^{3-}. The band marked with an * originates from the solvent water

Figure 3-24 shows the experimental (of a solution at pH 13.00 where L^{4-} is present at maximum concentration) and calculated Raman spectrum of L^{4-}. It has the simplest spectrum of all the protonated forms of HEDP and assignment is therefore quite straightforward for this totally deprotonated form of HEDP. Similar to H_2L^{2-} and HL^{3-}, it was found that the broad band centred at ~1105 cm^{-1} collectively represents the vibrations associated with the νPO, νC-C and δCC-O modes or mixtures thereof. The dramatic increase in intensity of the $\nu^{S}PO_3^{2-}$ band at 989 cm^{-1} is a direct result of the two PO_3^{2-} moieties becoming chemically equivalent, similar to the solid-state case for anhydrous HEDP, but probably also symmetrically equivalent due to the dynamic nature of the solution environment. As mentioned previously, the comparison of H_3L^- and H_4L was complicated by the fact that the experimental Raman spectra overlap closely, and it was not possible to obtain pure species spectra to compare with the theoretically calculated data.

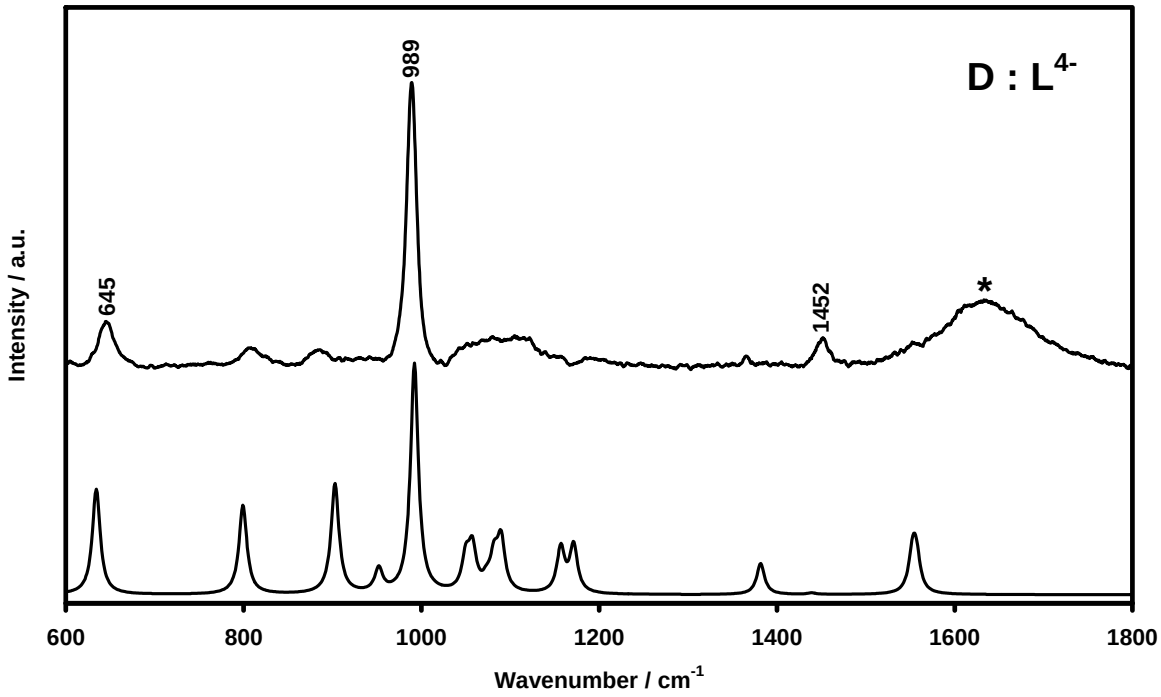

Figure 3-24. Comparison between the experimental and theoretically calculated Raman spectra for L^{4-}. The band marked with an * originates from the solvent water

The solid-state structure of $CaH_2L{\cdot}2H_2O$ makes for an interesting comparison with conformer B_b of H_2L^{2-}. The orientation of the $^-O\text{-}P\cdots P\text{-}O^-$ moiety in B_a is not suitable for chelation with an M^{2+} cation, even though it is the lowest energy conformer in solution, as evidenced by the experimental and theoretical data. The question therefore arises as to what the preferred conformer for coordination with M^{2+} could be. Using the solid-state crystal structure conformation of CaH_2L as input for the optimisation and Raman spectrum calculation in solution generates two *i*-wavenumbers and has a O=P···P=O dihedral angle of 134.4º, which indicates that it is not the preferred conformer for chelation in solution. If the Ca-chelated conformer B_b is used as input, a vibrational analysis is obtained with no *i*-wavenumbers and a O=P···P=O dihedral angle of 49.1º, indicating that it is probably the conformer required for chelation with Ca^{2+}. This implies that conformer B_a has to go through a transition state to become B_b, to coordinate with Ca^{2+}. In summary, conformer B_a is the uncoordinated conformer of $H_2L^{2-}(aq)$ and B_b the required higher energy, coordinating conformer of H_2L^{2-} in solution. Unfortunately, due to the insolubility of $CaH_2L{\cdot}2H_2O$, no experimental data could

be obtained for $CaH_2L(aq)$ to compare with the calculated Raman spectrum to confirm this postulation.

3.5.2 Solid-state Raman spectroscopy of CaHEDP salts

During the investigation of the interaction of 0.5 M and 0.005 M HEDP(aq) solutions with hydroxyapatite, two CaHEDP complexes were spectroscopically observed to form at the solid-solution interface. One was identified and characterised as $CaH_2L{\cdot}2H_2O$. Unfortunately, the other could not be isolated for characterisation, but the Raman spectrum could be obtained and is assigned. As stated in Section 2.2, the single crystal of $CaH_2L{\cdot}2H_2O$ used for XRD analysis was also used to obtain its reference Raman spectrum. In this section the analysis of only the Raman spectra will be discussed, and the nature of interaction in Chapter 4. Figure 3-25 shows the Raman spectra of the two macroanatomical types of bone, trabecular (cancellous) and compact (cortical) [26] in comparison with HA and $CaHPO_4$. The main bands are indicated to serve as a guide, but all bands have been assigned in Tables 3-15 and 3-16.

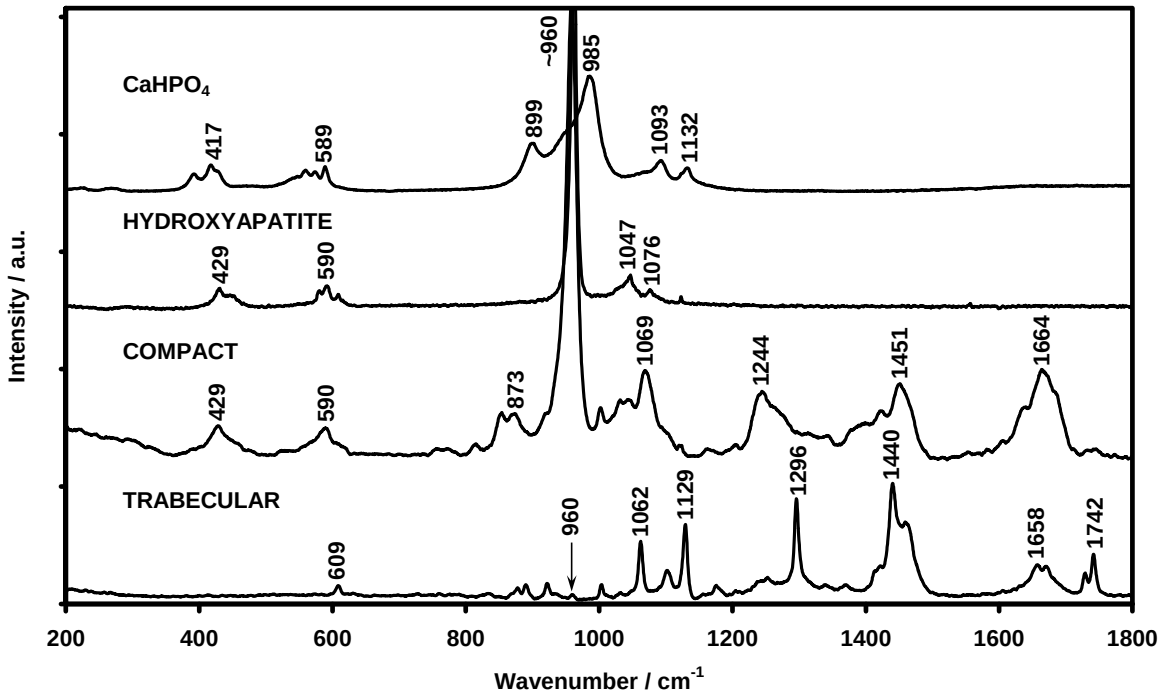

Figure 3-25. The Raman spectra of trabecular and compact bone, HA and $CaHPO_4$ for the region 200 – 1800 cm^{-1}

The difference between the Raman spectra of the trabecular and compact bone is very notable. This can be ascribed to the fact the calcium phosphate apatitic mineral is the dominant component in the compact bone, whereas the trabecular bone is much more organic in nature [26]. The organic components, such as collagen, remaining lipids and blood, dominate its Raman spectrum to such an extent that the most intense band of HA at 960 cm^{-1} is hardly visible. The majority of bands observed above 1100 cm^{-1} are assigned to this organic phase in trabecular bone. Penel *et al*. [27] have done a comprehensive assignment and discussion of the Raman spectra of the organic phase found in bone, and therefore the assignment of the organic phase's Raman bands observed on compact and trabecular (porous) bone during this study is given in Table 3-15, but will not be discussed in detail.

Figure 3-26 shows the comparative Raman spectra of $CaH_2L{\cdot}2H_2O$, the unknown Ca-HEDP complex and $HEDP{\cdot}H_2O$. Many vibrational bands are observed for all three compounds, but three non-overlapping bands were identified by which the compounds could be used to monitor the formation or disappearance of the Ca complexes as HEDP is added to the surface of bone, HA or $CaHPO_4$. These bands are assigned to the ν^{s}C-P, ν^{s}P-O(H) and δPO-H/ν^{as}P-O(H) vibrations and are: 627, 972 and 1036 cm^{-1} for $HEDP{\cdot}H_2O$; 641, 963 and 1072 cm^{-1} for $CaH_2L{\cdot}2H_2O$; and 658, 946 and 1088 cm^{-1} for the unknown Ca-HEDP complex. Similar to the analysis of the HEDP(aq) spectra, the bands assigned to the ν^{s}P-O(H) and δPO-H/ν^{as}P-O(H) vibrations show the most dramatic shift due to the change in the P-O bond order [30], which is in turn due to either the different modes of Ca^{2+} coordination or the degree of deprotonation. Other bands could probably also be used to differentiate between the three compounds, but might not be observed if they are present at lower concentrations. These can be used as a secondary means of confirmation when observed.

The vibrational assignment of HA and $CaHPO_4$, as well as the full assignment of the Raman spectra obtained from $CaH_2L{\cdot}2H_2O$ and the unknown Ca-complex, can be found in Table 3-16. Hartree-Fock (HF) methods were selected for the molecular modelling of $CaH_2L{\cdot}2H_2O$, even though these methods do not take dynamic electron correlations into account (see Section 1.6.1.1 and Ref. [31]).

This was done as no initial geometrical optimisation was performed on the structure as determined from XRD, resulting in a less time-consuming calculation. Initial test calculations done on simpler, single molecules (relative to the $CaH_2L{\cdot}2H_2O$ unit cell) to compare the HF and B3LYP/DFT methods, in combination with various basis set combinations, ranging from 6-31G(d) – 6-311G++(2d,p); showed that the scaling factor required for the computed vibrational wavenumbers was the only dramatic difference between the two methods. Notably, because HF methods do not show a linear relation between the calculated and theoretical vibrational wavenumbers as the DFT methods do [32], only wavenumbers below 2000 cm^{-1} were assigned. Bands observed above 2000 cm^{-1} were assigned from literature sources (see Table 3-16).

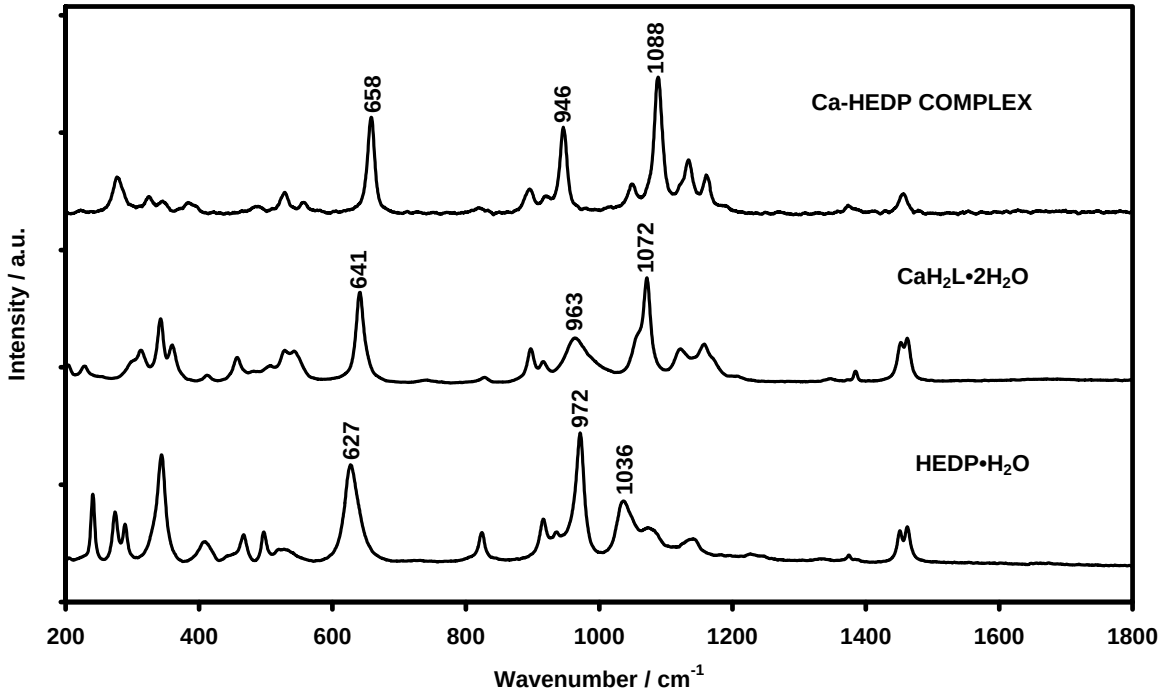

Figure 3-26. Comparative Raman spectra of HEDP, $CaH_2L{\cdot}2H_2O$ and the unknown Ca-HEDP complex. Unique non-overlapping bands are labelled

Table 3-15.

Assignment [27]	Bone Compact	Bone Porous	Assignment [27]	Bone Compact	Bone Porous	Assignment [27]	Bone Compact	Bone Porous
$\delta^{as}PO_4^{3-}$	429		νC-C trans (phospholipids, blood)		1062	νC=C (blood)	1636	
$\delta^{as}PO_4^{3-}$	590		$\nu^{as}PO_4^{3-}$ / νCO_3^{2-} B type	1069	1102	ν*cis*-C=C (lipids)		1658
$\delta^{as}PO_4^{3-}$		609	νCO_3^{2-} A type			Amide I-α helix	1664	
νCO_3^{2-} B type / νC-C-O (collagen)	767		νC-C (*trans*-phospholipids, proteins)		1129	Amide I (collagen)		1670
νC-C / νC-O-C (collagen)	813	836	ν^{s}C-O-C (proteins: Tyr, Phe) (collagen, lipids, blood)		1176	νC=OOC (collagen, lipid)	1744	1729 1742
δC-C-H_{ar} / (collagen, lipids)	854		Amide III-β (collagen, blood)	1244	1241 1253	νPO-H		2727
νC-C Ile / Val / Thr / Tyr (collagen, lipids)	873	878	δC=CH (phospholipids)		1296	$\nu^{s}CH_2$ (lipids)		2848
νP-OH / νC-C Pro ring (collagen, lipids)	922	922	Amide III-α helix (collagen, blood)		1339	$\nu^{as}CH_2$ (lipids) / $\nu^{s}CH_2$ (proteins)	2883	2883
νC-C_{aliph} Lys / Val / Leu (collagen)		935	Heme (collagen, blood)	1390		Heme (blood)		2915
$\nu^{s}PO_4^{3-}$	959	960	Heme (blood)	1422	1419	$\nu^{s}CH_3$ (proteins, lipids) / $\nu^{as}CH_2$ (proteins)	2942	2936
νHPO_4^{2-} / Phe (collagen, lipids)	1002	1004	δCH_2 (lipids)		1440	$\nu^{s}CH_3$ (lipids)		2958
$\nu^{as}PO_4^{3-}$	1042	1050	$\delta^{as}CH_3$ / δCH_2 (proteins, collagen, blood)	1451		$\nu^{s}CH_3$ (collagen, blood)	2978	
Pro / Phe / Tyr / Thr	1030	1032	δCH_2 (lipids)		1459	νC=CH (collagen, blood)	3066	3061

ν: stretch, δ: deformation; s: symmetrical, as: anti-symmetrical; ar: aromatic, aliph: aliphatic

Amino acids: Ile (isoleucine), Val (valine), Thr (threonine), Tyr (tyrosine), Lys (lysine), Leu (leucine), Pro (proline), Phe (phenylalanine)

CO_3^{2-} A type – CO_3^{2-} substituted in OH^- site of HA

CO_3^{2-} B type – CO_3^{2-} substituted in PO_4^{3-} site of HA

Table 3-16. Raman band assignments for $CaHPO_4$, $CaH_2L{\cdot}2H_2O$ and the unknown Ca-HEDP complex

Vibrational assignments†	Solid 'substrates'		HEDP complexes		
	$CaHPO_4$ [28]	HA [29]	Ca-complex	$CaH_2L{\cdot}2H_2O$ Exp.	Calc.
Probable lattice vibrations	140 w		114 vw	110 vw	
	180 w			121 vw	
	224 w		144 vw	149 w	
	268 w			170 w,sh	
			185 vw	182 w	
νOH…O				204 w	263
			223 vw	228 w	273
δC-C			277 m	254 vw	
				301 m,sh	
δOPO			326 w	313 m	311
			345 w	342 s	332
			383 w	360 m	355
				412 w	394
$\delta^{as}PO_4^{3-}$	392 m	431 m			
	417 m	447 m			
	428 m,sh				
δOPO				457 m	459
			487 w	482 w,sh	494
				506 w	513
			529 w	528 m	559
$\delta^{as}PO_4^{3-}$	539 m				
	560 m	580 m			
	573 m	592 m			
	589 m	608 w			
			557 w	543 m	589
νC-P			658 s	641 vs	643
				742 w,br	756
νC-C-O			819 w	828 w	871
$\nu^{as}PO_4^{3-}$	899 s				
νC-O-H			897 m	898 m	909
ν^{s}P-O(H)			920 m,sh	916 w	929
			946 s	963 m,br	1000
					1028
$\nu^{s}PO_4^{3-}$	958 s,sh	962 vs			
	985 vs				
$\nu^{as}PO_4^{3-}$	1065	1047 m			
	1093				
	1132				
δPO-H / ν^{as}P-O(H)			1049 m	1057 sh	1054
			1088 s	1072 vs	1076
$\nu^{as}PO_4^{3-}$		1076 w			
δCO-H			1134 m	1122 m	1116

Vibrational assignments†	Solid 'substrates'		HEDP complexes		
	$CaHPO_4$ [28]	HA [29]	Ca-complex	$CaH_2L \cdot 2H_2O$ Exp.	Calc.
νP=O / δPOH			1160 m	1158 m	1141
			1188 sh	1172 sh	1185
				1207 w	
$\delta^{s}CH_3$			1374 w	1373 vw	
				1385 w	
$\delta^{as}CH_3$			1456 m	1452 s	
				1462 s	
νPO-H			2725 w	2743 w	
$\nu^{s}CH_3$			2882 m,sh	2883 m	
			2887 m		
			2953 vs	2950 vs	
$\nu^{as}CH_3$				2983 sh	
				2991 s	
			3006 s,sh		
			3010 vs		
νO-H / νOH_2			3222 m	3224 vw,br	
				3354 w	
				3409 sh	
νO-H / HA		3578 s	3571 m		

† Bands that could be confidently assigned from the calculated spectra are given. Bands above 2000 cm^{-1} show a large scale factor error and are therefore not given as they could be confidently assigned from the literature [20–24].
ν: stretch, δ: deformation
s: symmetrical, as: anti-symmetrical
vw: very weak, w: weak, m: medium, s: strong, vs: very strong
sh: shoulder, br: broad

Three calcium complexes in solution have been identified for HEDP by means of glass potentiometric (GEP) studies, namely $CaHL^-$, Ca_2L and CaL^{2-}, for which the stability constants (log β) are 13.17, 9.53 and 5.34 respectively [5]. The fact that CaH_2L was not found by GEP, and the unknown complex formed (supposedly at lower HEDP concentrations) prompted the modelling of hypothetical solution compositions, using literature-reported data [5] and an assumed stability constant of the complex CaH_2L. The total Ca^{2+}(aq) concentration was allowed to vary over a wide range, between $1x10^{-3}$ and $1x10^{-7}$ M. The reason for this was that the stock HEDP solution was calcium-free and that most of the calcium leached from the solid phase (HA, bone, or CaHPO4) was instantly involved in the complex-formation reaction with HEDP, as evidenced by the Raman spectra in Figure 3-26. From the modelling results it appeared that the overall stability

constant (log β) for CaH_2L should be approximately 18. A selection of the modelled species distribution diagrams is shown in Figure 3-27 to facilitate the discussion. The species distribution diagram shown in Figure 3-27A (generated using the experimental conditions and stability constants of $CaHL^-$, Ca_2L, and CaL^{2-} [5] and CaH_2L, log β = 18.5) explains why the complex CaH_2L could not be obtained using GEP. CaH_2L is formed first (at lower pH values), but only to a small extent (only a small portion of the total calcium dissolved is in solution) and in the pH range where the H_2L^{2-} ligand is the dominant species present. The concentration of CaH_2L is therefore not significant enough to influence other Ca-HEDP equilibria dramatically. According to the reaction equation,

$$Ca^{2+} + H_2L^{2-} \rightarrow CaH_2L$$

there is no proton involved, and hence there is no change in the total free-proton concentration in a solution when only this complex is formed, and will therefore not be directly detected by GEP. Even though GEP is a powerful and versatile analytical technique for studying metal complexes, it is only successful when the free-proton concentration varies due to complex-formation reactions. Because CaH_2L is highly insoluble, it does not contribute to the change in free-proton concentration. Secondly, the species distribution diagrams in Figure 3-27 are for fully soluble Ca-HEDP systems, and even with this assumption CaH_2L is formed at very low concentrations as seen in Figure 3-27 A and 3-27B.

The complexes $CaHL^-$ and Ca_2L in Figure 3-27A start to form almost simultaneously in the pH range between 5 and 6, but Ca_2L forms predominantly in this region. When the total calcium concentration is decreased to $1x10^{-6}$ M and the total ligand concentration increased to 0.005 M (similar to the experimental conditions for the lower HEDP concentration of 0.005 M), then the solution composition changes dramatically (as can be seen in Figure 3-27B). Clearly, at the lower total metal ion concentration, the complex Ca_2L is not formed to any significant concentration level. $CaHL^-$ is the major calcium complex with only a small fraction of CaH_2L being formed. The results for an HEDP

concentration of 0.5 M can be seen in Figure 3-27C and represent the conditions of the experimental results when the formation of CaH_2L at very low pH was observed and the conditions under which the CaH_2L single crystal was obtained. Even at a high total metal ion concentration ($1x10^{-3}$ M), there is no evidence of Ca_2L formation. This strongly suggests that $CaHL^-$ is the unknown complex observed in the experimental Raman spectra obtained.

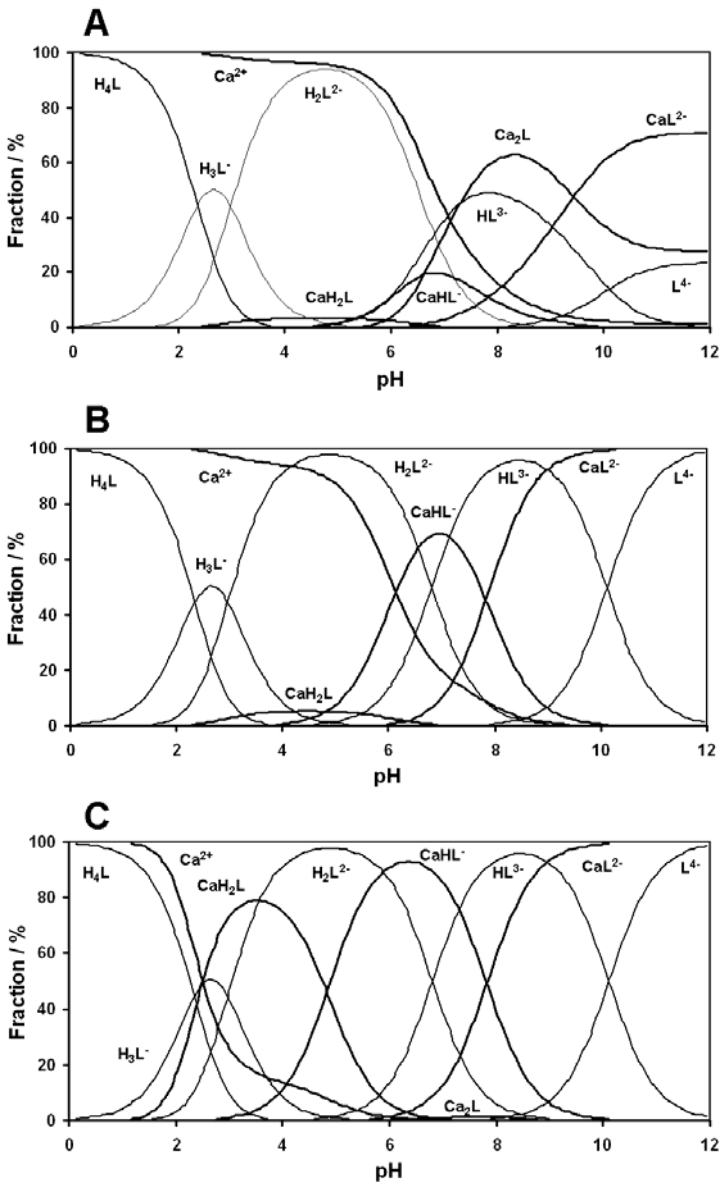

Figure 3-27. Species distribution diagrams of hypothetical, totally soluble Ca-HEDP systems generated under different total ligand and metal ion concentrations. A. $[L_T]$ = $1x10^{-3}$ M, $[M_T]$ = $9x10^{-4}$ M, log$\beta(CaH_2L)$ = 18.5; B. $[L_T]$ = $5x10^{-3}$ M, $[M_T]$ = $1x10^{-6}$ M, log$\beta(CaH_2L)$ = 18.0; C. $[L_T]$ = $5x10^{-1}$ M, $[M_T]$ = $1x10^{-3}$ M, log$\beta(CaH_2L)$ = 18.0

Further evidence that $CaHL^-$ is the unknown Ca complex can be found in the shift of the ν^sC-P band to a higher wavenumber as HEDP is deprotonated in solution [24] and as observed in this study. In Figure 3-26 the shift of this band occurs such that the wavenumber value of the unknown Ca-HEDP complex (658 cm^{-1}) is greater than that of $CaH_2L{\cdot}2H_2O$ (641 cm^{-1}), which in turn is greater than that of $HEDP{\cdot}H_2O$ (627 cm^{-1}) giving the series: unknown Ca-HEDP complex > $CaH_2L{\cdot}2H_2O$ > $HEDP{\cdot}H_2O$. The degree of protonation of $HEDP{\cdot}H_2O$ is greater than that of $CaH_2L{\cdot}2H_2O$, and if the shift of the ν^sC-P band is used as an indicator of the degree of deprotonation, we can write a deprotonation series, based on the ν^sC-P band position, of: $Ca_x(H_yL)_z{\cdot}nH_2O$ > $CaH_2L{\cdot}2H_2O$ > $H_4L{\cdot}H_2O$. For this series to be true, y = 0,1. However, y = 0 is not the most likely possibility as it is formed at high pH values, making y = 1 the likely candidate. To have a neutral solid present means the formula unit is $Ca_3(HL)_2{\cdot}nH_2O$, where n is unknown at this stage.

Attempts to increase the amount of this Ca-HEDP complex was done by adjusting the pH of an HEDP solution by addition of $Ca(OH)_2$(s). If the molar ratio of $Ca(OH)_2$:HEDP was 1:1, $CaH_2L{\cdot}2H_2O$ precipitated (confirmed by XRD), while a ratio of 2:1 gave a mixture of complexes that could not be resolved by XRD.

3.6 Multivariate curve resolution

The species distribution diagram of HEDP(aq) has been generated from experimental [5] data, as seen in Figure 3-16, for the pH region under investigation. As stated previously, it was not possible to resolve the pure spectra of H_4L and H_3L^- from the experimental data due to the species overlap associated with the pH region in which these species are shown to be at their maximum concentration. Multivariate curve resolution (MCR) was therefore utilised to attempt to distinguish the various species from one another. The region of 860 – 1280 cm^{-1} was selected as a suitable range in the Raman spectra for MCR analysis as it contains the bands associated with the PO_3H_2 moieties that vary with pH. The bands below this range were weak and, due to the high fluorescence background observed in the lower wavenumber region, it was

suspected that they would introduce errors into the MCR analysis. Particular bands such as the ν^{s}C-P stretch at ~640 cm^{-1}, which exhibits a small but constant shift over the pH range, for example, could result in each spectrum being identified as a separate component. The region above 1280 cm^{-1} contains bands assignable to the aqueous medium, as well as bands associated with the methyl vibrations that overlap with these water bands, and it was thus also deemed unnecessary to include this region.

Therefore, if a hydrogen-bonded system were to exist at low pH and high HEDP concentration, and were to contribute significantly to the Raman spectra, one could expect MCR analysis to find a six-component system when considering the total residuals of the MCR fitting. If such a hydrogen-bonded system does not contribute to the Raman spectra, one should determine only a five-component system, which represents the five protonated/deprotonated forms of HEDP. Also, each of the components is known from Figure 3-16 to have only one pH region of maximum concentration, and they can therefore not be observed more than once. Therefore the unimodal constraint [33] of MCR was also investigated.

Figure 3-28 shows the MCR-determined species distribution diagrams for a six-component system calculated multimodally and unimodally. By comparing the six-component species distribution diagrams in Figure 3-28A and 3-28B, it can be seen that a species is present which closely overlaps with the region where H_2L^{2-} is expected (blue line in Figure 3-28A), or a species is present simultaneously with H_3L and H_2L (red line in Figure 3-28B). The two unknown species are also present in pH regions where the hydrogen-bonded species are not expected. Therefore this confirms that a six-component analysis does not correctly describe the system. Therefore a hydrogen-bonded species does not contribute significantly enough to the experimental data set to be observed as a separate species.

The five-component multimodal and unimodal analyses both show very good agreement with the experimentally generated species distribution diagram, as can be seen in Figure 3-29A and Figure 3-29B respectively, two anomalies (marked *) are observed in Figure 3-29A. When considering only the species

distribution diagrams, it could be deduced that unimodality is a valid assumption as it is the best fit for the experimentally generated species distribution diagram, as seen in Figure 3-29B. Comparison of both the multimodal and unimodal MCR analyses generated with the experimental spectra obtained at pH values where each protonated form of HEDP is at its maximum concentration, as shown in Figures 3-30A and 3-30B respectively, shows good agreement for H_2L^{2-}, HL^{3-} and L^{4-}.

The discrepancies again arise in the cases of H_4L and H_3L^-. The experimental Raman spectrum at pH 0.98 is predicted to have an H_4L/H_3L^- ratio of approximately 3:2, indicating that both species will be observed simultaneously and that not all bands in the experimental Raman spectrum of H_4L can be assigned to H_4L only. For the unimodal result of H_4L, as seen in Figure 3-30B, it can be clearly seen that this MCR analysis associates all the bands observed experimentally as originating from H_4L, which is unlikely. In the multimodal case, seen in Figure 3-30A, we see that both H_4L and H_3L^- contain bands in their experimental Raman spectra that can be assigned to the pure component generated spectra of H_4L and H_3L^- as being contaminants, which is a much more realistic view of the species that are really present.

With regard to Figure 3-29A, the two anomalies (marked *) occurring in the multimodal case are thought to result from possible hydrogen-bonded species that manifest themselves in this fashion, rather than being detected as a formal species during the six-component MCR analysis. More evidence to support this possible hydrogen bonding can be found in the paper by Zeevaart *et al.* [5] on an H_6L^{2+} species that could be reinterpreted as strong hydrogen bonding rather than the presence of a formal species.

In summary, it seems that the deprotonation of HEDP over the pH range studied is well described as being a five-component system, with strong anecdotal evidence that hydrogen bonding occurs. This results in the generation of anomalies in the pure component distribution diagram as obtained by MCR analysis.

Unfortunately, these pure component spectra still seem to contain hydrogen bonding contributions associated with each separate protonated form, and they therefore do not compare well with the modelled vibrational data as the system modelled does not take intermolecular hydrogen bonding between two H_4L or H_3L^- units into account.

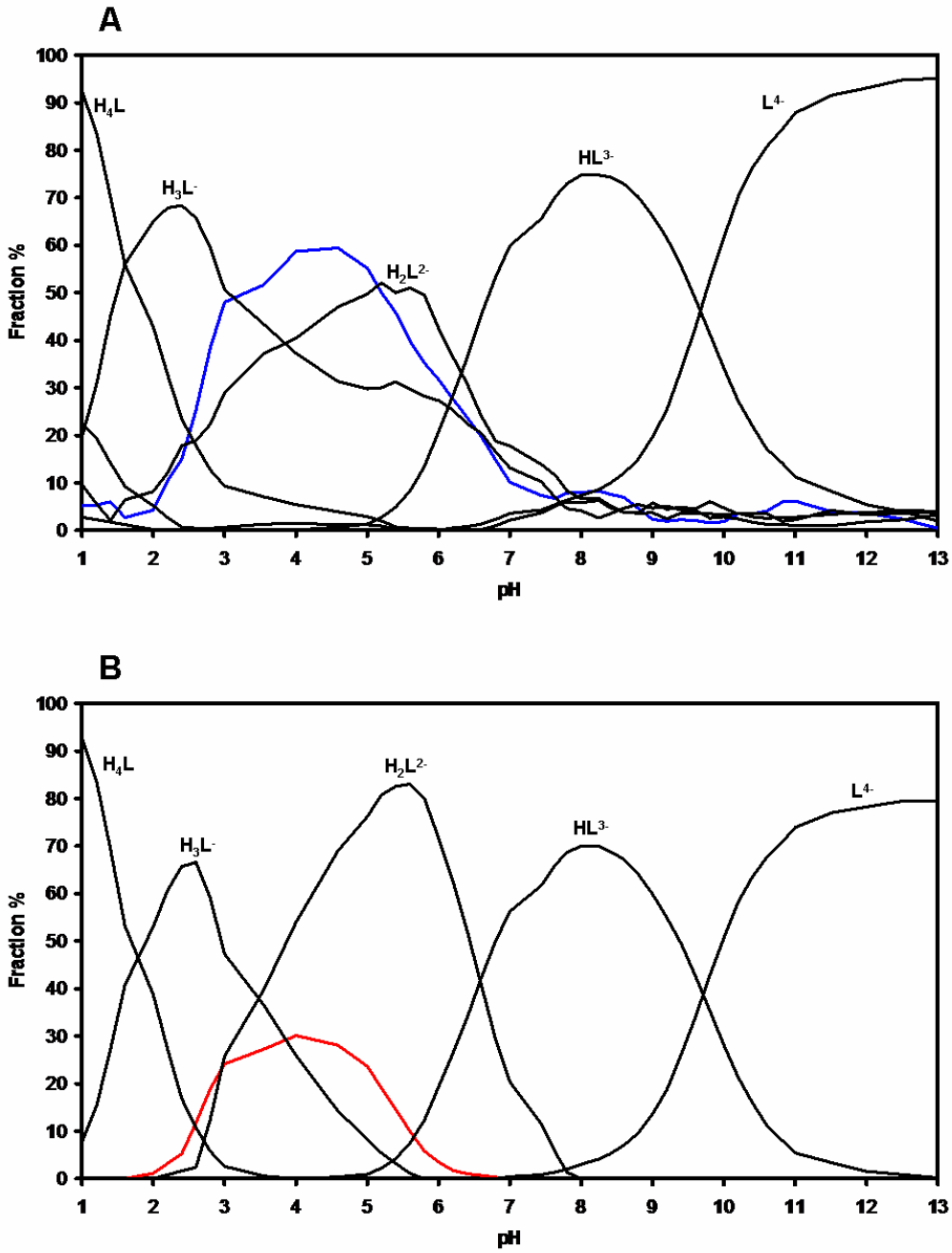

Figure 3-28. The six-component MCR species distribution diagram for HEDP calculated A. multimodally and B. unimodally. The component in blue and red is the sixth, unknown component

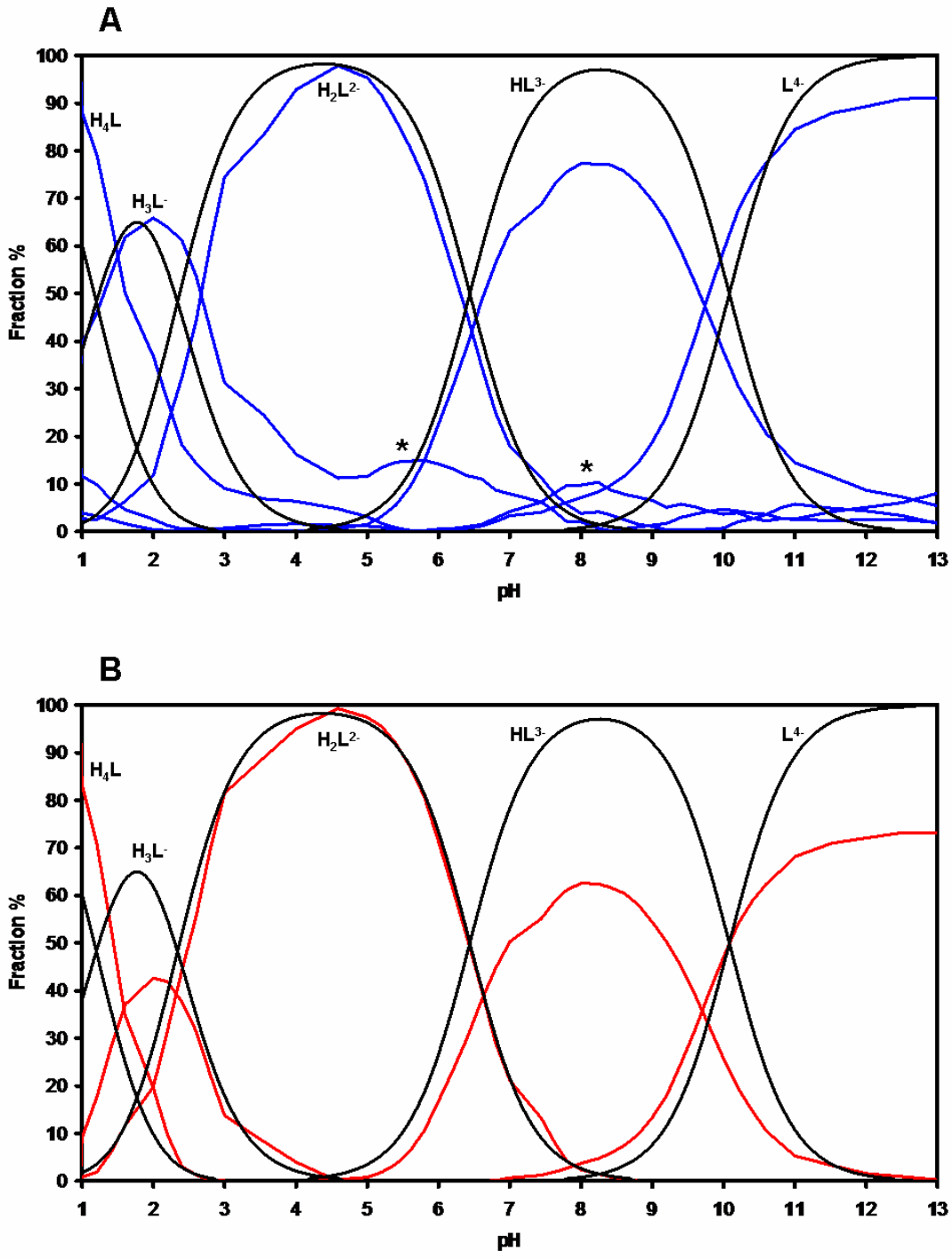

Figure 3-29. The five-component MCR species distribution diagram for HEDP calculated A. multimodally (in blue) and B. unimodally (in red). Both are superimposed on the experimentally generated species distribution curve (in black) for comparison. Anomalies marked with an * are discussed in the text

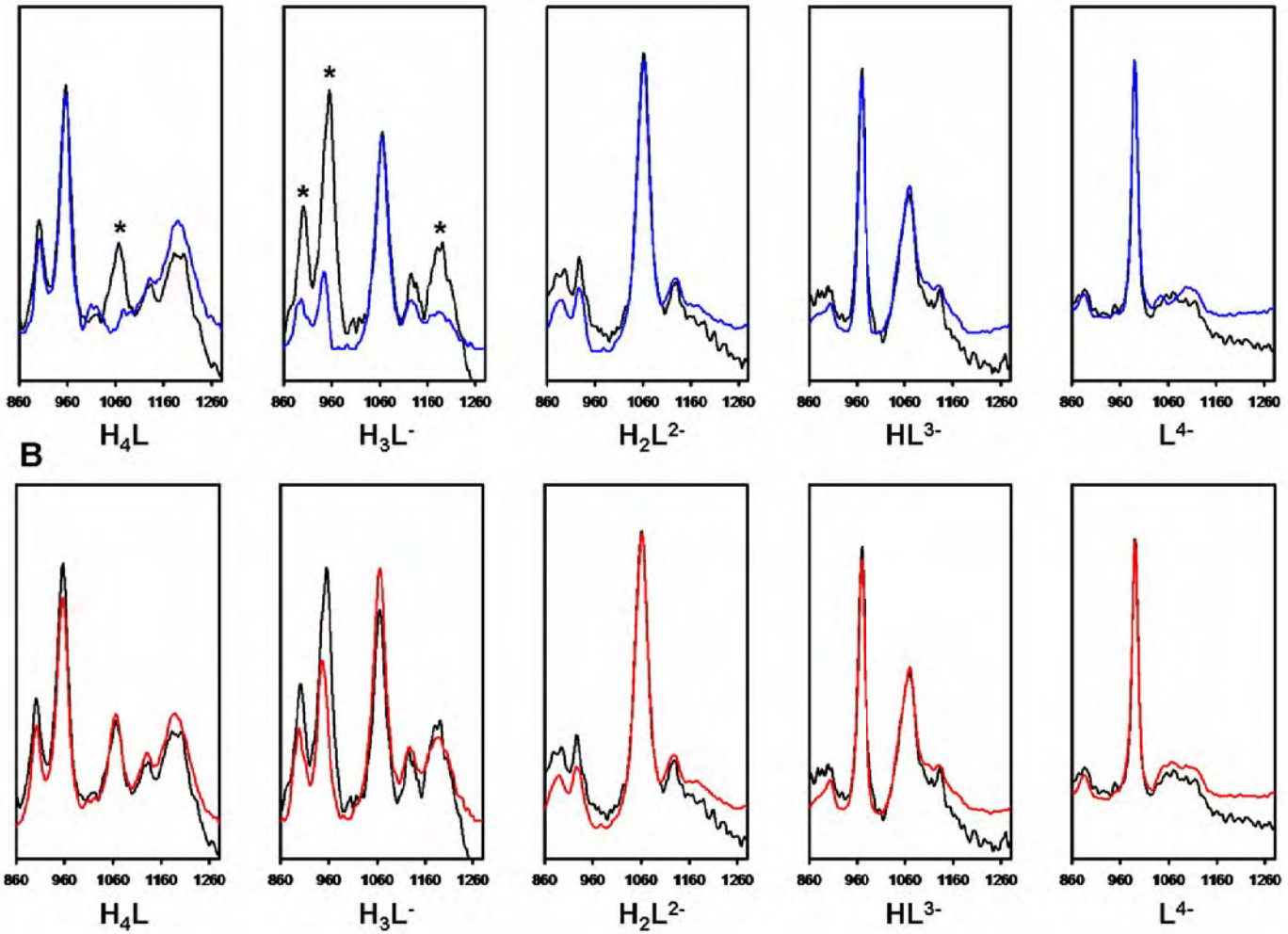

Figure 3-30. A. Multimodal (blue) and B. unimodal (red) generated pure component Raman spectra in comparison with experimental Raman spectra taken at pH values where each species is present at maximum concentration. The contamination of H_4L and H_3L^- can be clearly seen and the contaminant bands are marked with an *

3.7 Conclusions

It was illustrated in this chapter that various spectroscopic techniques can be used to obtain different, complimentary and supporting information regarding HEDP, its protonated forms and their conformers. Each technique gave different information regarding the nature of the structure and conformeric interactions. The use of molecular modelling to support what was observed shows that theoretical methods can be used to aid in the interpretation of HEDP's experimental data. This leads to a better understanding of HEDP, its various protonated forms and their conformers' interaction in solution, solid state and solid-solution interface that will be discussed in Chapter 4.

3.8 References

[1] E. Guenin, E. Degache, J. Liquier, M. Lecouvey. *Eur. J. Org. Chem.* **2004**, 2983.

[2] R.K. Harris, L.H. Merwin, G. Hägele. *Z. Naturforsch. B*, **1989**, *44*, 1407.

[3] R.K. Harris, L.H. Merwin, G. Hägele. *J. Chem. Soc., Faraday Trans.* **1989**, *85*, 1409.

[4] K. Popov, L.H.J. Lajunen, A. Popov, H. Rönkkömäki, M. Hannu-Kuure, A. Vendilo. *Inorg. Chem. Comm.* **2002**, *5*, 223.

[5] J.R. Zeevaart, N.V. Jarvis, I. Cukrowski, G.E. Jackson. *S. Afr. J. Chem.* **1997**, *50*, 189.

[6] E.G. Afonin, G.G. Aleksandrov. *Russ. J. Gen Chem.* **2003**, *73*, 340.

[7] A.J. Collins, G.W. Frasier, P.G. Perkins, D.R. Russell. *J. Chem. Soc., Dalton Trans.* **1974**, 960.

[8] V.A. Uchtman, R.A. Gloss. *J. Phys. Chem.* **1972**, *76*, 1298.

[9] J.P. Silvestre, N.Q. Dao, Y. Leroux. *Heteroatom Chem.* **2001**, *12*, 73.

[10] J.P. Silvestre, N.Q. Dao, G. Heger, A. Cousson. *Phosphorus Sulfur* **2002**, *177*, 277.

[11] A.J. Florence, K. Shankland, T. Gelbrich, M.B. Hursthouse, N. Shankland, A. Johnston, P. Fernandes, C.K. Leech. *Cryst. Eng. Comm.* **2008**, *10*, 26.

[12] N. Redman-Furey, M. Dicks, A. Bigalow-Kern, R.T. Cambron, G. Lubey, C. Lester, D. Vaughn. *J. Pharm. Sci.* **2005**, *94*, 893.

[13] A.A. Coelho, *J. Appl. Cryst.* **2000**, *33*, 899.

[14] V. Gogonea, C. Bãleanu-Gogonea, E. Osawa. *Theochem*. **1998**, *432*, 177.

[15] T. Ida, M. Ando, H. Toraya. *J. Appl. Cryst.* **2000**, *33*, 1311.

[16] A. Coelho. *Topas Academic Version 4.1 – Technical Reference*, **2007**, Chapter 12.

[17] R.A. Young (Ed.). *The Rietveld Method*, Oxford University Press, Oxford, **1996**.

[18] V.A. Uchtman. *J. Phys. Chem.* **1972**, *76*, 1304.

[19] G. Fiquet, P. Richet, G. Montagnac. *Phys. Chem. Miner.* **1999**, *27*, 103.

[20] D. Lin-Vien, N.B. Colthup, W.G. Fateley, J.G. Grasselli. *The Handbook of Infrared and Raman Characteristic Frequencies of Organic Molecules*, Academic Press Inc., London, **1991**, Chapters 2, 4 & 16.

[21] K. Nakamoto. *Infrared and Raman Spectra of Inorganic and Coordination Compounds,* 5th Edition, John Wiley & Sons, Chichester, **1997**, Part A.

[22] L.A. Myund, E.A. Bus'ko, N.I. Smirnova, S.N. Terekhin, N.M. Dyatlova, K.A. Burkov. *Vestn. Lenin U. Fiz. Kh. Seriya 4*, **1987**, *3*, 48.

[23] E.A. Bus'ko, L.A. Myund, S.N. Terekhin, K.A. Burkov, N.M. Dyatlova, N.A. Volkova. *Zh. Neorg. Khim.* **1988**, *33*, 603.

[24] L.A. Myund, E.A. Bus'ko, S.N. Terekhin, K.A. Burkov. *Vestn. Lenin U. Fiz. Kh. Seriya 4*, **1990**, *1*, 33.

[25] G.E. Walfaren. *J. Phys Chem.* **1990**, *94*, 2237.

[26] J.H. Lin. *Bone*, **1996**, *18*, 75.

[27] G. Penel, C. Delfosse, M. Descamps, G. Leroy. *Bone*, **2005**, *36*, 893.

[28] F.S. Casciani, R.A. Condrate. *Proc. Int. Congr. Phosphorous Compds*, **1980**, *2*, 175.

[29] G. Penel, G. Leroy, C. Rey, B. Sombret, J.P. Huvenne, E. Bres. *J. Mater. Sci., Mater. Med.* **1997**, *8*, 271.

[30] L. Popović, D. De Waal, J.C.A. Boeyens. *J. Raman Spectrosc.* **2005**, *36*, 2.

[31] K.V. Berezin, V.V. Nachaev, T.V. Krivokhizina. *Mol. Spectrosc.* **2003**, *94*, 398.

[32] K.V. Berezin, V.V. Nachaev. *J. Appl. Spectrosc.* **2004**, *71*, 164.

[33] R. Tauler, A. de Juan. In *A Practical Guide to Chemometrics*, P. Gemperline (Ed.). Taylor and Francis: CRC Press, New York, **2006**. Chapter 11.